

Article

Paleoproterozoic Multiple Tectonothermal Events in the Longshoushan Area, Western North China Craton and Their Geological Implication: Evidence from Geochemistry, Zircon U–Pb Geochronology and Hf Isotopes

Renyu Zeng ^{1,2,3}, Jianqing Lai ^{1,2,*}, Xiancheng Mao ^{1,2}, Bin Li ^{1,2}, Jiandong Zhang ^{1,2}, Richard C. BAYLESS ^{2,4} and Lizhi Yang ^{1,2}

¹ Key Laboratory of Metallogenic Prediction of Nonferrous Metals and Geological Environment Monitoring, Ministry of Education, Central South University, Changsha 410083, China; zengrenyu@126.com (R.Z.); xcmiao@126.com (X.M.); cutelb@126.com (B.L.); csuzjd@sina.com (J.Z.); yanglizhidz@csu.edu.cn (L.Y.)

² School of Geosciences and Info-Physics, Central South University, Changsha 410083, China; richardbayless02@gmail.com

³ State Key Laboratory Breeding Base of Nuclear Resources and Environment, East China University of Technology, Nanchang 330013, China

⁴ Department of Natural Sciences, Shawnee State University, Portsmouth, OH 45662, USA

* Correspondence: ljq@csu.edu.cn; Tel.: +86-138-7598-3805

Received: 12 July 2018; Accepted: 9 August 2018; Published: 21 August 2018



Abstract: The Alxa block is located in the southwestern margin of the North China Craton. The Paleoproterozoic tectonic evolution, crustal growth and tectonic affinity of the block remain unknown or controversial. The Longshoushan (LS) area is one of the few areas that outcrop Paleoproterozoic to crystalline basement rocks in the Alxa Block. In this study, we present whole-rock geochemistry, zircon U–Pb geochronology and Lu–Hf isotope data from metagabbro, metadiorite, quartz syenite, granitic leucosome and pegmatoid leucosome in the LS area. These rocks all are enriched in LREE and LILE, and depleted in HREE and HFSE. Eight new LA-ICP-MS zircon U–Pb ages yielded three magmatic ages of 2044 Ma, 2029 Ma and 1940 Ma, and three metamorphic ages of 1891 Ma, 1848 Ma and 1812 Ma. Lu–Hf analyses reveal that the magmatic zircons and anatectic/metamorphic zircons from all the rock types are characterized by positive $\epsilon_{\text{Hf}}(t)$ (−0.16 to 10.89) and variable $\epsilon_{\text{Hf}}(t)$ (−11.21 to 6.24), respectively. Based on the previous studies and our new data, we conclude that the LS area experienced three magmatic events (2.5–2.45 Ga, ~2.1–2.0 Ga and ~1.95–1.91 Ga) and three regional metamorphism/anatexis events (~1.93–1.89 Ga, ~1.86–1.84 Ga and ~1.81 Ga) in Paleoproterozoic. The age–Hf isotope data establishes two main crustal growth events at ~2.9–2.5 Ga and ~2.2–2.0 Ga in the LS area. These data indicate that the LS area experienced intraplate extensional setting in the middle Paleoproterozoic, and continental subduction, collision and exhumation in the late Paleoproterozoic. Combining the geochronological framework and tectonic evolution, we suggest that the Alxa Block is part of the Khondalite Belt.

Keywords: North China Craton; Alxa Block; Longshoushan area; zircon U–Pb geochronology; Hf isotopes; Paleoproterozoic

1. Introduction

The North China Craton (NCC) is the largest and oldest cratonic block in China. Recent studies show that the NCC does not have a single basement, rather, it formed from an amalgamation of micro

blocks [1,2]. The tectonic division scheme, formation and evolution of these micro blocks remain controversial [1–17]. However, the cratonization of the NCC is considered to have occurred during Neoproterozoic to Paleoproterozoic time. Hence, the Neoproterozoic–Paleoproterozoic evolution of the NCC is the theoretical foundation for solving the problems above.

The research degrees on the westernmost NCC, termed the Alxa block, is low in the study of other parts of the NCC. The Neoproterozoic–Paleoproterozoic tectonic evolution and crustal growth events of the Alxa block remain controversial. It is still at issue whether or not the Alxa block exists Archean rocks [18–22]. Furthermore, although it is generally accepted that the Alxa Block is an integrated part of the NCC during the Paleoproterozoic nowadays [1,19,21,23], the tectonic affinity of the Alxa Block is still controversial and leads to two different opinions: (1) it is part of the Khondalite Belt (also known as the Inner Mongolia Suture Zone [24]) [19,21,25]; or (2) it is the western extension of the Yinshan Block [1,3,4]. As one of the few areas where the Archean to Paleoproterozoic basement rocks outcrop in the Alxa Block, the Longshoushan (LS) area is important to the understanding of Neoproterozoic–Paleoproterozoic evolution of the Alxa block. A series of new geochronology data indicate that the LS area experienced multiple tectonothermal events during the Paleoproterozoic [19,23,26–28]. This provides a basis for research on the tectonic evolution, crustal growth and tectonic affinity of the Alxa Block. However, previous research focused on the chronology of the Paleoproterozoic rocks, and were rarely concerned with the study on their geochemistry and petrogenesis.

In order to better understand the geological implication of the Paleoproterozoic rocks, we carried out a detailed field, petrological, whole-rock geochemistry and in situ zircon U–Pb and Hf isotopic investigations on five Paleoproterozoic rocks in the LS area. The aims of this work are to (1) precisely determine the protolith and/or metamorphic ages and petrogenesis of these rocks; (2) elucidate the geochronological framework, crustal growth and tectonic evolution of the LS area during the Paleoproterozoic; (3) and subsequently explore the tectonic affinity of the Alxa Block.

2. Geological Setting

The Alxa Block is located in the westernmost part of the NCC, and together with the Yinshan Block, Ordos Block and Khondalite Belt, formed the Western Block of the NCC [1]. This block is in fault contact with the North Qilian Orogenic Belt to the south and the Tarim Craton to the west, and bounded by the Central Asian Orogenic Belt in the north (Figure 1a). Generally, the Archean to Paleoproterozoic basement rocks of Alxa Block are mainly distributed in the Debushige area, Bayan-Wulashan area, Beidashan area and LS area.

The LS area extends as a long, narrow, NW-trending strip in the southwest of the Alxa Block (Figure 1a). This area is bounded by faults against the Hexipu corridor transitional zone to the south. The Chaoshui basin is located between the LS area and the parallel Beidashan area (Figure 1b). The main outcropping stratum of the area are the LS Group, the late Mesoproterozoic Dunzigou Group [29] and the Neoproterozoic–Cambrian Hanmushan Group [30,31]. As the basement rock, the LS Group is exposed in a long narrow belt about 500 km long and 30 km wide bounded by 38–40° N latitude and 99–103° E longitude in the LS area [32]. It is in unconformable contact with the overlying strata of the Dunzigou Group. The LS Group underwent deformation, regional metamorphism and migmatization [32]. It mainly consists of schlieren and homogenic migmatites, marble, biotite-plagioclase gneiss, granulites, quartz schist, amphibolite and pyroclastic rock.

Intrusive rocks, ranging in composition from ultramafic to felsic, are widespread in the LS area. The ages of magmatic activities are from the Paleoproterozoic to Neoproterozoic and are concentrated in the Paleoproterozoic and the Paleozoic [19,20,26,27,33–36]. The remarkable Jinchuan ore-bearing mafic to ultrabasic rocks formed at 800–850 Ma [37–39].

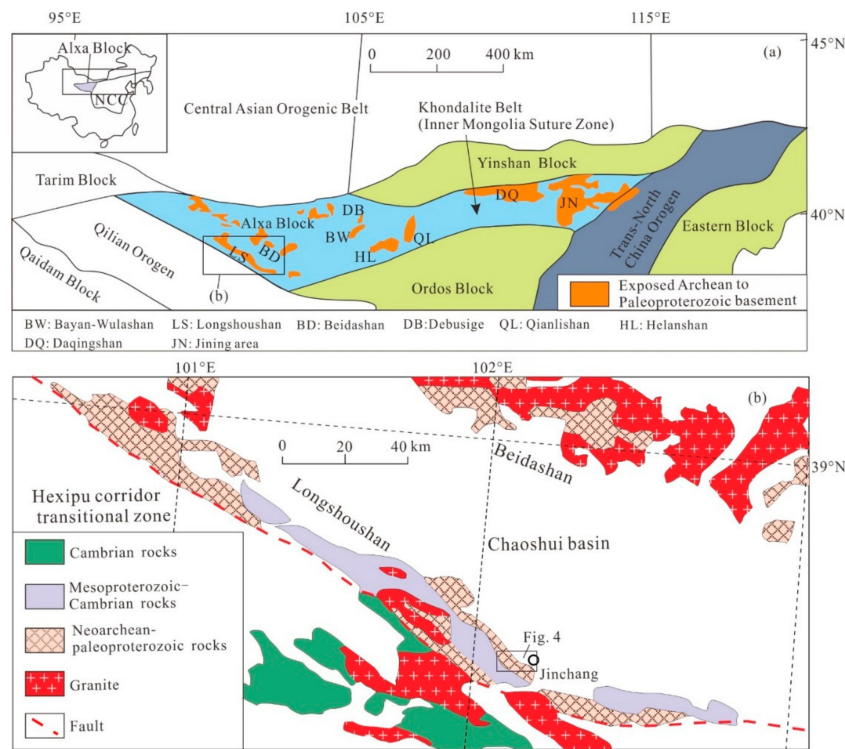


Figure 1. (a) Tectonic subdivision of the North China Craton (NCC) (modified from [25]); (b) Geological sketch map showing the geological setting of the LS area (modified from [21]).

3. Field Relationship and Sample Descriptions

Samples collected from the Jinchuan mining area, or nearby, in the LS Group. The rock types analyzed in this study for geochemistry, zircon U–Pb geochronology and Lu–Hf isotopes include metagabbro, metadiorite, quartz syenite, granitic leucosome and pegmatoid leucosome. The rock types and summary of mineral assemblages are given in Table 1 and the rock locations are shown in Figure 2. The zircon crystals of metagabbro and metadiorite were separated from three approximately 20 kg rock samples (JZ-12, JC-119 and JC-32), respectively. A brief description of the rock types and their petrography is given below.

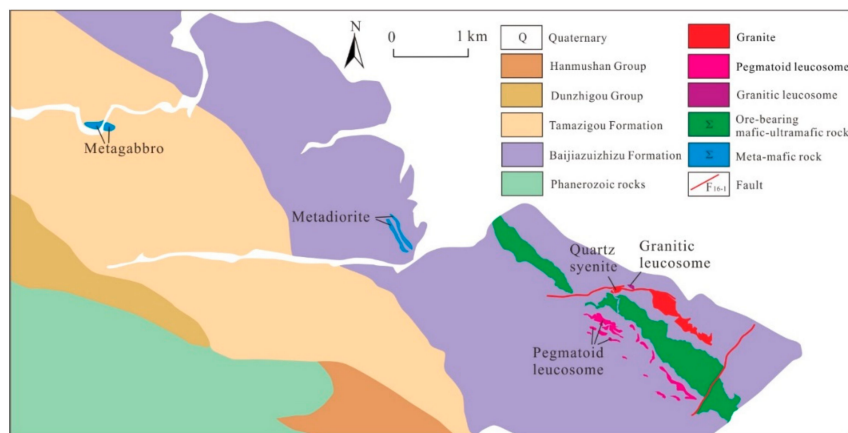


Figure 2. Geologic map of the Jinchuan mineral area.

Table 1. Modal abundance (%) of minerals for different rock types in LS area.

Sample Number	Lithology	Texture	Modal Abundance (%)								
			Px	Ol	Am	Q	Kfs	Pl	Bt	Ms	Hem
JZ-15	metagabbro	medium-coarse grained texture	40	10	10			35	5		
JZ-113	metadiorite	porphyroblastic texture			30	5		45	15		
JZ-30	quartz syenite	medium-fine grained textures				18	60	10	4		8
JZ-36	granitic leucosome	porphyritic texture				40	35	23		2	
JZ-69	pegmatoid leucosome	pegmatitic and graphic textures				20	65	9	6		

Q—quartz; Kfs—feldspar; Pl—plagioclase; Bt—biotite; Ms—Muscovite; Hem—Hematite; Mag—Magnetite; Px—Pyroxene; Ol—Olivine; Am—Amphibole.

3.1. Metagabbro

The metagabbro dikes examined in this study occur in a swarm ~5 km northwest of the Jinchuan mining area (Figure 2). The rocks consist of several small metagabbro intrusions, which are commonly 10–50 m wide and 30–150 m long. They intruded into graphite marble and mica schist of the Tamazigou Formation (Figure 3a). These rocks are generally brown to dark green in color and are medium-coarse grained ($d = 3\text{--}7\text{ mm}$). In thin section, the rocks are composed of pyroxene (~40%), plagioclase (~35%), olivine (~10%), amphibole (~10%) and biotite (~5%) with some rutile and magnetite as accessory. The pyroxene, olivine and amphibole have been largely tremolitization, serpentinitization, steatitization and chloritization (Figure 3b). The biotite has been largely replaced by muscovite. The plagioclase is generally altered to sericite and zoisite.

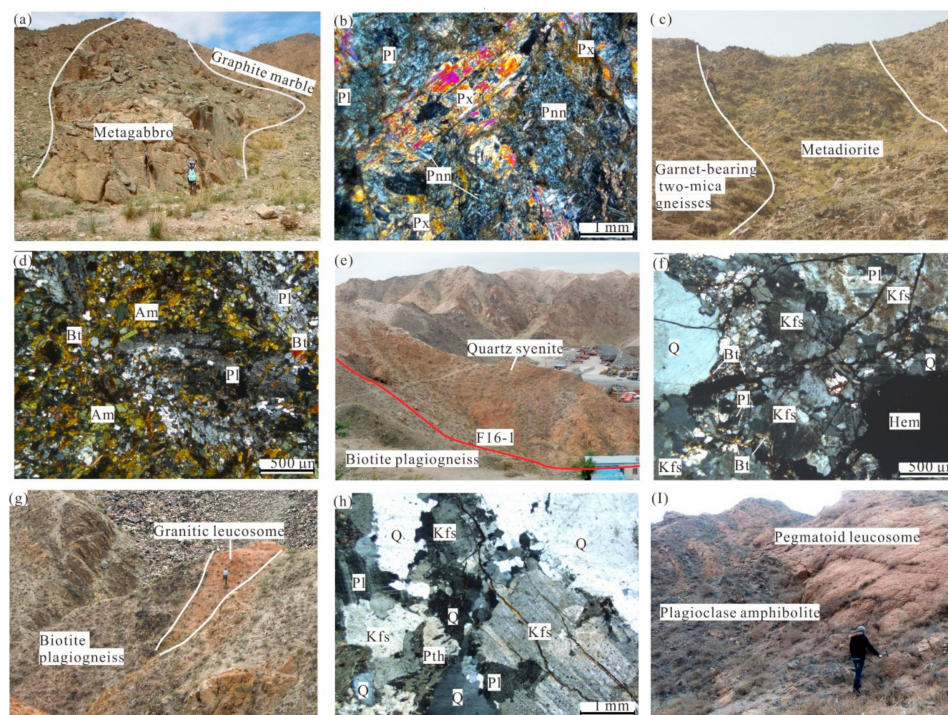


Figure 3. Field aspects and photomicrographs of Paleoproterozoic rocks: (a) metagabbro dike intruding graphite marble; (b) metagabbro sample JZ-15 (perpendicular polarized light); (c) metadiorite dike intruding garnet-bearing two-mica gneisses; (d) metadiorite sample JC-116 (perpendicular polarized light); (e) quartz syenite in fault contact with the biotite plagiogneiss; (f) quartz syenite sample JZ-30 (perpendicular polarized light); (g) Granitic leucosome vein intruding biotite plagiogneiss; (h) Granitic leucosome sample JZ-36 (perpendicular polarized light); (i) gradational contact relationship between pegmatoid leucosome and schlieren migmatite. Mineral abbreviations are as follows: Am, amphibole; Pnn, pennine; Px, pyroxene; Bt, biotite; Q, quartz; Kfs, K-feldspar; Pl, plagioclase; Hem, hematite.

3.2. Metadiorite

Two parallel dikes of metadiorite are up to 15 m width and extend more than 1 km in NW direction in the west of the Jinchuan mining area (Figure 2). They intruded into garnet-bearing two-mica gneisses of the Baijiazui Formation (Figure 3c). The rocks are grayish-green in color, with porphyroblastic texture. Plagioclase (~45%), amphibole (~30%), biotite (~15%), quartz (~5%) and opaque minerals (~5%) are the dominant minerals. Porphyroblastic are plagioclase, and the grain size mainly ranges between 1.5–2.5 mm. The matrix is mainly composed of amphibole, biotite and quartz, the grain size mainly ranges between 0.2–0.4 mm. The porphyroblastic plagioclase contains a large number of fine-grained amphibole and biotite inclusions in the core (Figure 3d).

3.3. Quartz Syenite

The quartz syenite is located in the middle of the Jinchuan mining area and has an outcrop area of ~3 km² (Figure 2). The quartz syenite intruded into marble of the Baijiazui Formation, except on the northern side where it is in fault contact with the biotite gneiss of the Baijiazui Formation (Figure 3e). The syenite is generally pale brown, medium-fine grained texture. The major minerals are K-feldspar (~60%), quartz (~18%), plagioclase (~10%), hematite (~8%) and biotite (~4%). Hematite fills in the cracks and crystals usually appear in groups. Small biotites fill in the interstices between the other minerals (Figure 3f).

3.4. Granitic Leucosome

The veins and lenses of the granitic leucosome are widely distributed within the biotite plagiogneiss (melanosome) of the Baijiazui Formation in the middle of the Jinchuan mining area (Figure 2). The largest vein, which is oriented NW-SE, ~120 m in length and 10–30 m in width (Figure 3g). The rocks are pale yellow with porphyritic and a fine-grained matrix (Figure 3g). The dominant minerals are quartz (~40%), K-feldspar (~35%), plagioclase (~23%), with lesser muscovite (~2%). Quartz crystals have anhedral form, wavy extinction and indented boundaries (Figure 3h).

3.5. Pegmatoid Leucosome

The schlieren-homogenic migmatite of the Baijiazui Formation is located in the south part of the Jinchuan mining area (Figure 2). In this formation, pegmatoid leucosome occurs as interlayers, irregular-shaped veins and lentoid in plagioclase amphibolite (melanosome) of the Baijiazui Formation (Figure 3i). The pegmatoid leucosome is generally pale red in color and with coarse-grained texture. They contain K-feldspar (~65%), quartz (~20%), plagioclase (~9%) and minor biotite (~6%), with accessory magnetite, apatite and zircon. The K-feldspar crystals can vary up to 6 cm in size, and the quartz crystals mainly range between 0.4–0.8 cm. Small biotites fill in the interstices between the other minerals and crystals usually appear in groups.

4. Analytical Methods

4.1. Whole-Rock Major and Trace Elements

Major oxide concentrations were measured by X-ray fluorescence (XRF) spectrometry at Analytical Chemistry and Testing Services (ALS) Chemex Co Ltd. (Stafford, Australia). Fused glass disks with Lithium Borate were used and the analytical precisions were better than ±0.01%, estimated from repeated analyses of the standards GSR-2 and GSR-3. Trace elements were detected using the lithium borate dissolution method and ICP-MS. Analyses of United States Geological Survey rock standards (BCR-2, BHVO-1 and AGV-1) indicate precision and accuracy are better than ±5% for trace elements.

4.2. Zircon U–Pb Dating

Zircon U–Pb dating analyses of JZ-12 (metagabbro), JZ-31 (quartz syenite) and JZ-38 (granitic leucosome) were performed at the Key Laboratory of Crust-Mantle Materials and Environments of Chinese Academy of Sciences at the University of Science and Technology of China (USTC), using an inductively-coupled plasma mass spectrometer (LA–ICP–MS; Perkin Elmer Elan DRC II) equipped with a Microlas system (GeoLas 200 M, 193 nm ArF excimer laser). Zircon 91500 and SRM610 were used as the external standards for U–Pb isotope ratios and element content, respectively. The spot diameter of laser ablation pits is 32 μm and the average power output about 4 W. For detailed instrument parameters and analysis processes refer to [40].

U–Pb dating analysis of JC-119 (metadiorite) and JZ-70 (pegmatoid leucosome) was performed at Nanjing FocuMS Contract Testing Co. Ltd, using Teledyne Cetac Technologies Analyte Excite laser-ablation system (Bozeman, MT, USA) and Agilent Technologies 7700x ICP-MS (Hachioji, Tokyo, Japan). The 193 nm ArF excimer laser, homogenized by a set of beam delivery systems, was focused on zircon surfaces with the fluency of 6.0 J/cm². Ablation protocol employed a spot diameter of 35 μm at 8 Hz repetition rate for 40 s (equating to 320 pulses). Helium was applied as a carrier gas to efficiently transport aerosol to the ICP-MS. Zircon 91500 was used as the external standard to correct instrumental mass discrimination and elemental fractionation. Zircon GJ-1 was treated as quality control for geochronology. Lead abundance of zircon was externally calibrated against NIST SRM 610 with Si as the internal standard, while Zr was used as the internal standard for other trace elements.

Processing software of U/Pb is LaDating (version 1.5), quantitative calibration for Pb isotope dating was performed by ComPbcorr#3_18 [41], and concordia diagrams and weighted mean calculations were performed using Isoplot 4.15 [42].

4.3. Zircon Lu–Hf Isotopes

In-situ Hf ratio analyses of JZ-12 (metagabbro), JZ-31 (quartz syenite) and JZ-38 (granitic leucosome) were measured at the Advanced Analytical Centre at James Cook University, using a 193-nm ArF laser and Thermo Scientific Neptune multicollector ICPMS. Spot sizes were 60 μm , with a 4-Hz laser pulse repetition rate. Ablation was conducted in He gas flow. The Mud Tank reference zircon (MTZ) and the Geostandard FC1 zircon were used as the external standards, and the ¹⁷⁶Hf/¹⁷⁷Hf ratios of these two external standards are 0.282184 and 0.282507, respectively [43]. In the experiment, standard zircon MTZ and FC1 were analyzed, and the ¹⁷⁶Hf/¹⁷⁷Hf ratios were 0.282148–0.282175 and 0.282488–0.282502 respectively, in accordance with the recommended value.

In-situ Hf ratio analyses of JC-119 (metadiorite) and JZ-70 (pegmatoid leucosome) were measured at Nanjing FocuMS Contract Testing Co. Ltd. (Nanjing, China) and Teledyne Cetac Technologies Analyte Excite laser-ablation system (Bozeman, MT, USA) and Nu Instruments Nu Plasma II MC-ICP-MS (Wrexham, Wales, UK) were combined for the experiments. Spot sizes were 50 μm , with an 8-Hz laser pulse repetition rate. Helium was applied as the carrier gas to efficiently transport aerosol to MC-ICP-MS. Three standard zircons, GJ-1, 91500, and Penglai, were treated as quality control every ten unknown samples. The ¹⁷⁶Hf/¹⁷⁷Hf ratios of GJ-1, 91500, and Penglai is 0.282012 [44], 0.282307 \pm 0.000031 [45] and 0.282906 \pm 0.000010 [46], respectively. In the experiment, standard zircon GJ-1, 91500, and Penglai were analyzed, and the ¹⁷⁶Hf/¹⁷⁷Hf ratios were 0.281957–0.282022, 0.282274–0.282362 and 0.282891–0.282921 respectively, in accordance with the recommended value.

5. Analytical Results

Supplementary Materials Tables S1–S3 list the data of major and trace elements, zircon U–Pb ages, and Hf isotopes.

5.1. Geochemical Characteristics

5.1.1. Meta-Mafic Rocks

Five samples of metadiorite and eight samples of metagabbro were analyzed. Due to the high LOI value, element contents of metagabbro are normalized to 100% on an LOI free basis in all diagrams. The metadiorite and metagabbro show limited variation in SiO₂ contents (45.28–49.63%). The Na₂O/K₂O ratios of all the samples are more than 1.0. The MgO content and Mg# value of the two are different, the samples of metagabbro have high content of MgO (23.62–31.99%) and Mg# value (78.90–83.46%), whereas the samples of metadiorite have low content of MgO (4.06–4.14%) and Mg# value (33.78–34.60%). In the Zr/TiO₂-Nb/Y discrimination diagram (Figure 4a), all samples of metagabbro fall in the Andesite/Basalt field, whereas the samples of metadiorite fall in the Subalkaline Basalt field. In the SiO₂-TFeO/MgO discrimination diagram (Figure 4b), the samples of metagabbro are “Calc-Alkaline series”, and the samples of metadiorite are “Tholeiitic series”.

In the chondrite-normalized REE patterns (Figure 5a,c), all samples are fractionated with LREE enrichment (La_N/Yb_N varying between 2.32 to 7.81). The samples of metagabbro display clearly negative Eu anomalies (δEu = 0.38–0.73), whereas the samples of metadiorite have δEu ≈ 1 (±0.1). In the primitive mantle-normalized trace element diagram (Figure 5b,d), all samples show enrichment of La and LILEs (e.g., Rb, Ba, K) and slight depletion of HFSEs (e.g., Nb, Ta, Ti, Zr and Hf).

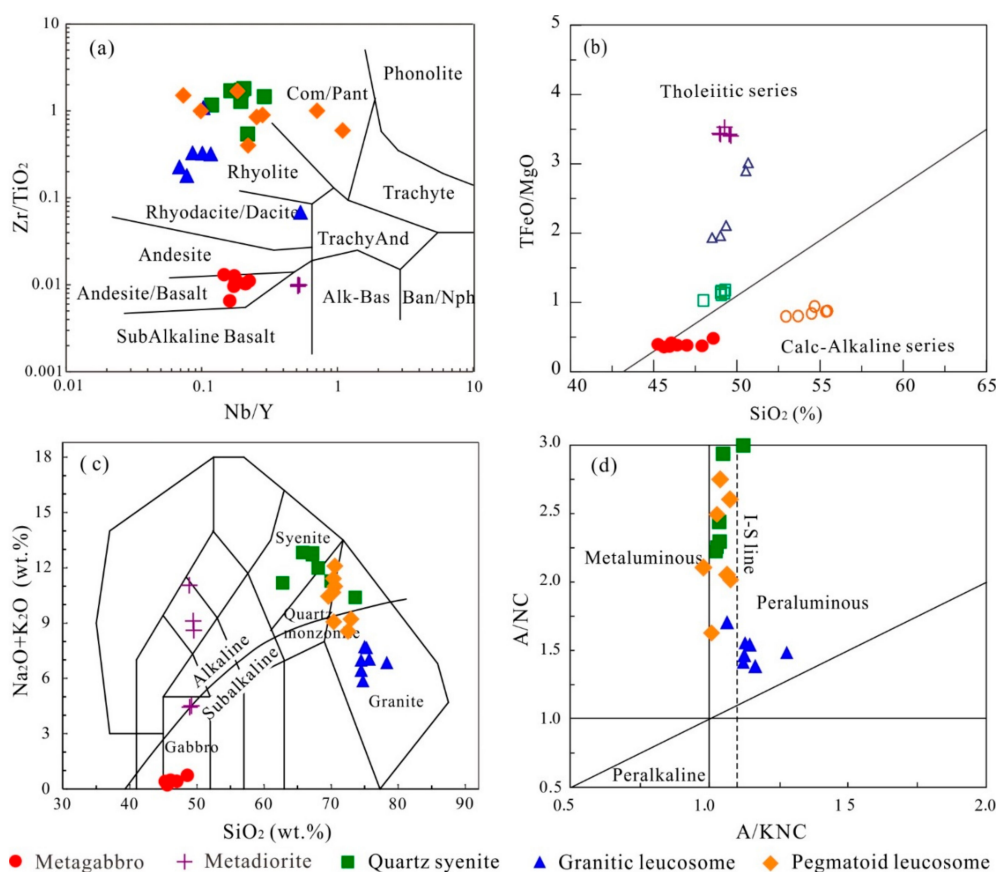


Figure 4. (a) Nb/Y-Zr/TiO₂ (modified from [47]); (b) SiO₂-TFeO/MgO (modified from [48]); (c) SiO₂-MALI diagram (modified from [49]); (d) A/KNC-A/NC diagram (modified from [50]).

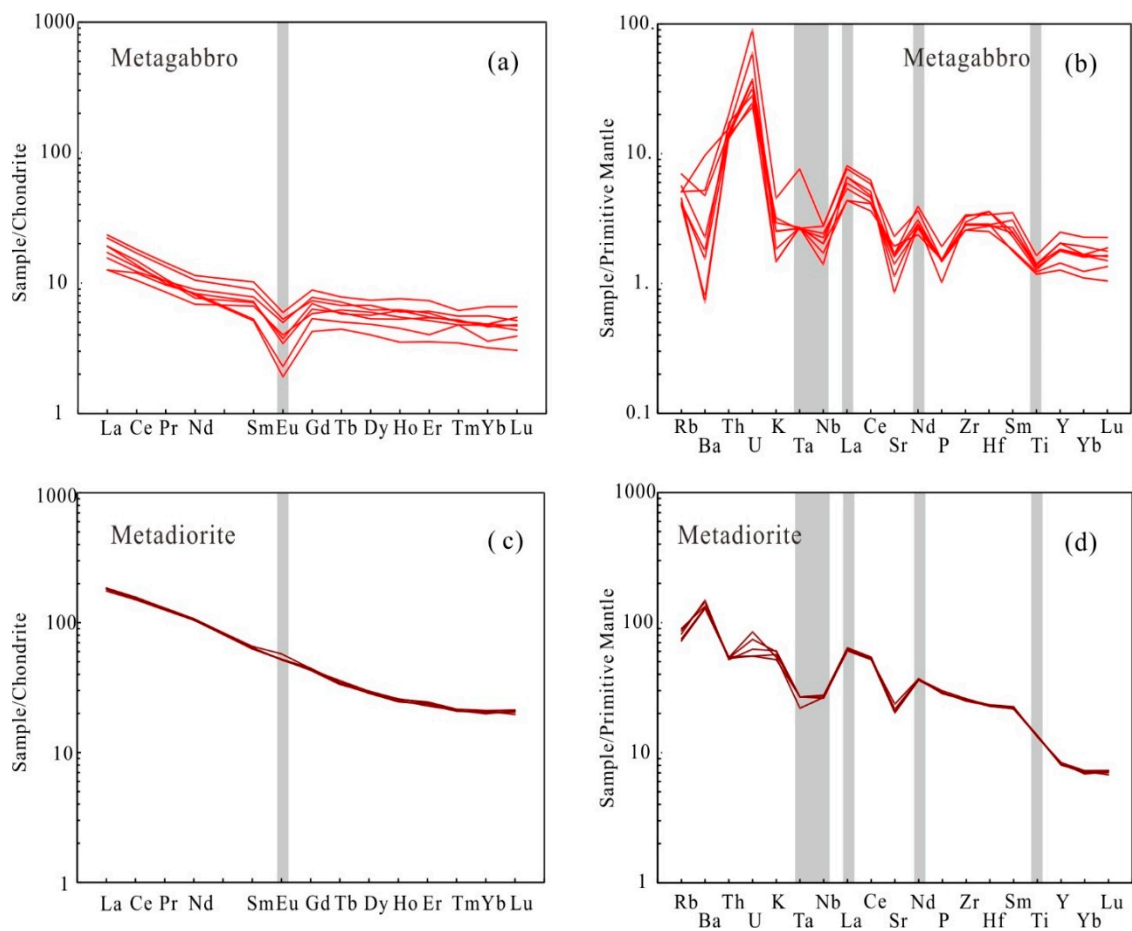


Figure 5. Chondrite-normalized REE patterns (a,c) and primitive mantle-normalized trace element patterns (b,d) of meta-mafic rocks (chondrite and primitive mantle values are from [51]).

5.1.2. Quartz Syenite

The seven samples of quartz syenite have SiO_2 contents from 62.80 to 74.10% (average 67.90%). They have low Na_2O (1.26–4.50%), high K_2O (7.76–10.05%) and total alkalis ($\text{Na}_2\text{O} + \text{K}_2\text{O}$) contents of 10.39 to 12.81% (average 11.87%). All samples but two fall into the syenite field in the SiO_2 -MALI diagram (Figure 4c). Contents of Al_2O_3 are of 13.60 to 17.30% (average 15.93%), A/KNC are of 1.02 to 1.12 (average 1.04). All samples are weakly peraluminous in the A/NC-A/KNC diagram (Figure 4d).

The La_N/Yb_N values of quartz syenite range from 14.59 to 41.26 (average 28.57), showing enrichment of LREE and depletion of HREE (Figure 6a). All samples display clearly negative Eu anomalies ($\delta\text{Eu} = 0.38\text{--}0.73$) and no Ce anomalies ($\delta\text{Ce} = 0.93\text{--}1.07$). In the primitive mantle-normalized trace element diagram (Figure 6b), the samples show enrichment of La, Nd and LILEs (e.g., Rb, U, K) and slight depletion of HFSEs (e.g., Nb, Ta, Ti and P), and no depletion of Hf and Zr.

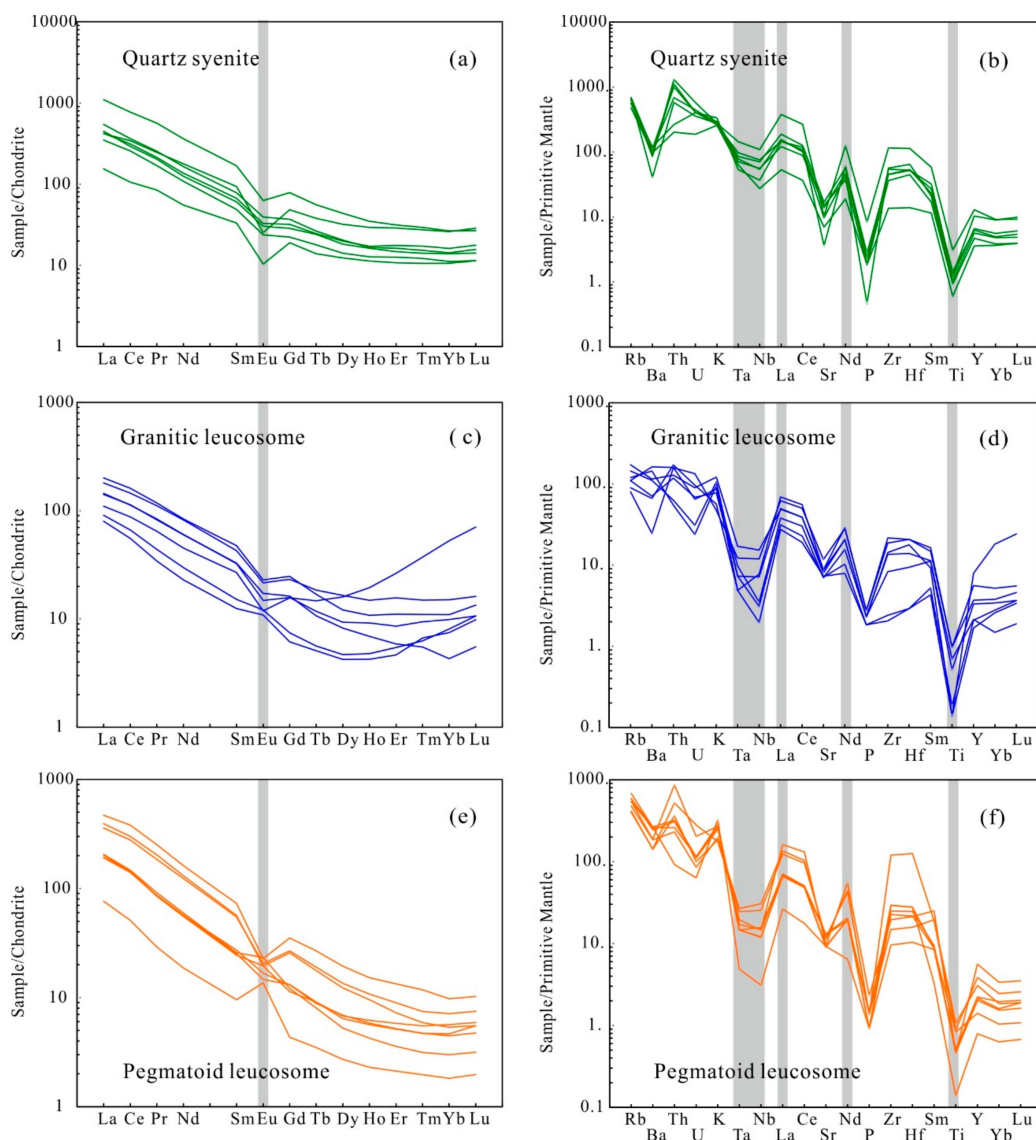


Figure 6. Chondrite-normalized REE patterns (a,c,e) and primitive mantle-normalized trace element patterns (b,d,f) of quartz syenite and leucosome (chondrite and primitive mantle values are from [51]).

5.1.3. Leucosome

Seven samples of granitic leucosome and eight samples of pegmatoid leucosome have been used for geochemical studies. The granitic leucosome and pegmatoid leucosome have high SiO_2 contents from 74.26 to 78.30% (average 75.36%) and 69.70 to 73.08% (average 71.00%), respectively. The samples of granitic leucosome have high Na_2O (3.21–4.83%), low K_2O (1.42–3.66%) and total alkalis ($\text{Na}_2\text{O} + \text{K}_2\text{O}$) contents of 5.90 to 7.72% (average 6.95%). The samples of pegmatoid leucosome have low Na_2O (2.29–3.82%), high K_2O (5.27–9.86%) and total alkalis ($\text{Na}_2\text{O} + \text{K}_2\text{O}$) contents of 8.58 to 12.12% (average 10.33%). In the SiO_2 -MALI discrimination diagram (Figure 4c), all samples of granitic leucosome and pegmatoid leucosome fall in or near the granite field. The samples of granitic leucosome have Al_2O_3 contents from 11.50 to 14.65%, A/KNC of 1.07 to 1.28, and are peraluminous in the A/NC-A/KNC diagram (Figure 4d). Meanwhile, the samples of pegmatoid leucosome have Al_2O_3 contents from 13.99 to 15.56%, A/KNC of 0.98 to 1.08, and are weakly peraluminous in the A/NC-A/KNC diagram (Figure 4d) except one.

The La_N/Yb_N values of granitic leucosome and pegmatoid leucosome range from 2.09 to 32.92 and 35.79 to 73.23, showing strong enrichment of LREE and depletion of HREE especially the latter

(Figure 6c,e). All samples display variable Eu anomalies ($\delta\text{Eu} = 0.45\text{--}2.12$) and slight positive Ce anomalies ($\delta\text{Ce} = 1.02\text{--}1.14$). In the primitive mantle-normalized trace element diagram (Figure 6d,f), all samples show enrichment of La, Nd and LILEs (e.g., Rb, Ba, U, K) and strong depletion of HFSEs (e.g., Nb, Ta, Ti and P), and no depletion of Hf and Zr.

5.2. Zircon U–Pb and Hf Isotopes

Zircon U–Pb dating and Hf isotopic composition were performed on samples JZ-12, JC-119, JC-32, JZ-31, JZ-38 and JZ-70. Cathodoluminescence (CL) images of these zircons are shown in Figure 7. As shown in Figure 8, most of these analyses are discordant, possibly resulting from Pb loss. Hence, the crystallization age of rocks are used to calculate their zircon $\varepsilon\text{Hf}(t)$ values. The $\varepsilon\text{Hf}(t)$ values of inherited/captured zircons are calculated using their U–Pb ages.

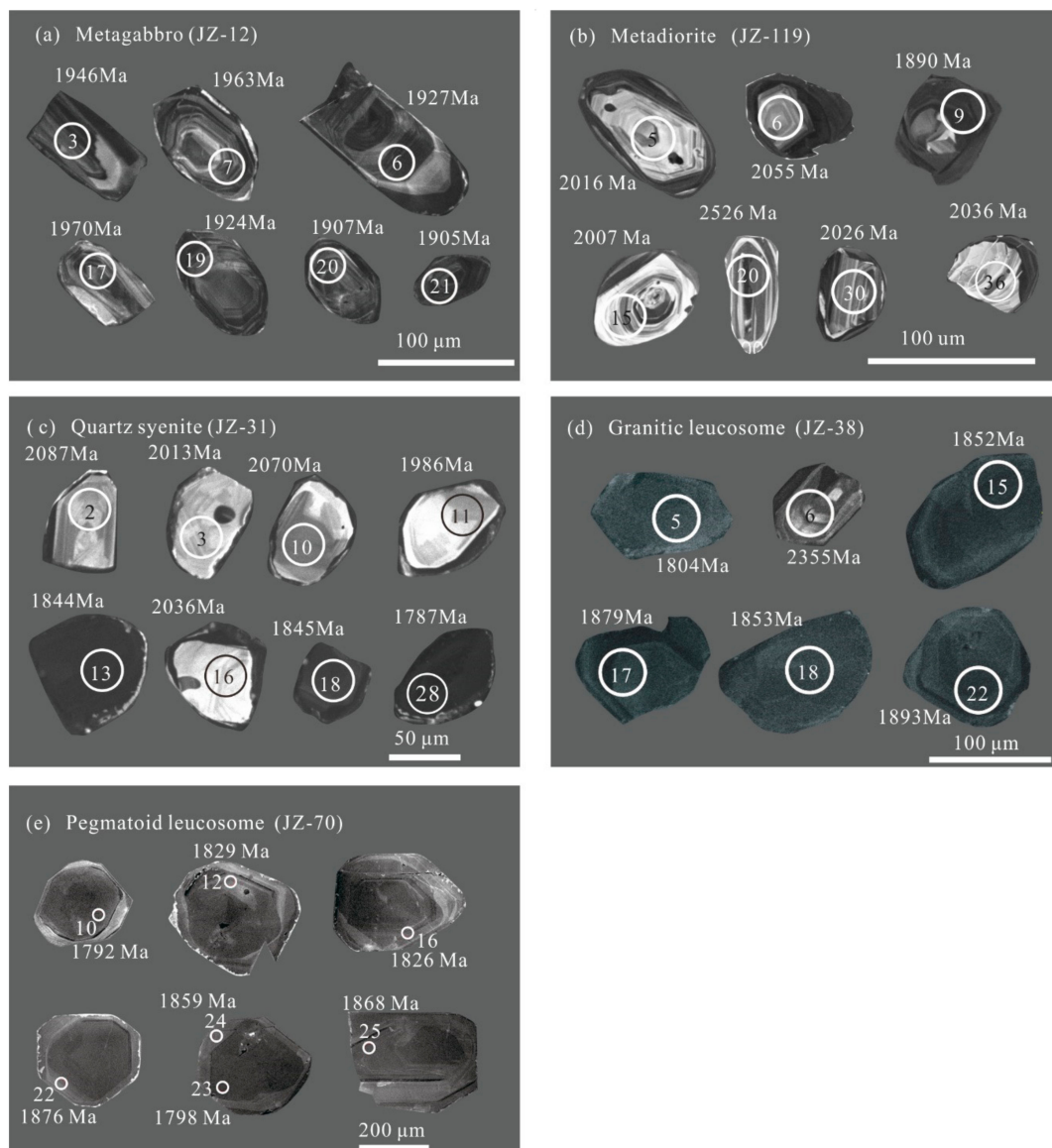


Figure 7. CL images of zircons. (a) Metagabbro sample JZ-12; (b) metadiorite sample JC-119; (c) quartz syenite sample JZ-31; (d) granitic leucosome sample JZ-38; (e) pegmatoid leucosome sample JZ-70. Circles denote U–Pb analysis spot. Numbers in the circles are the spot numbers. Numbers near the analytical spots are the U–Pb ages (Ma).

5.2.1. Metagabbro (JZ-12)

Zircons in JZ-12 are generally broken, but many still indicate an original long prismatic-shape (Figure 7a). Most zircon grains display widely spaced oscillatory zoning textures in CL images with Th/U values of 0.16 to 0.48. Twenty analytical spots yield a concordia upper intercept age of 1940 ± 16 Ma (MSWD = 0.59) (Figure 8a). This result is consistent with the weighted mean $^{207}\text{Pb}/^{206}\text{Pb}$ ages of 1940 ± 16 Ma (MSWD = 0.71), which is yielded from eighteen (nearly) concordant analyses.

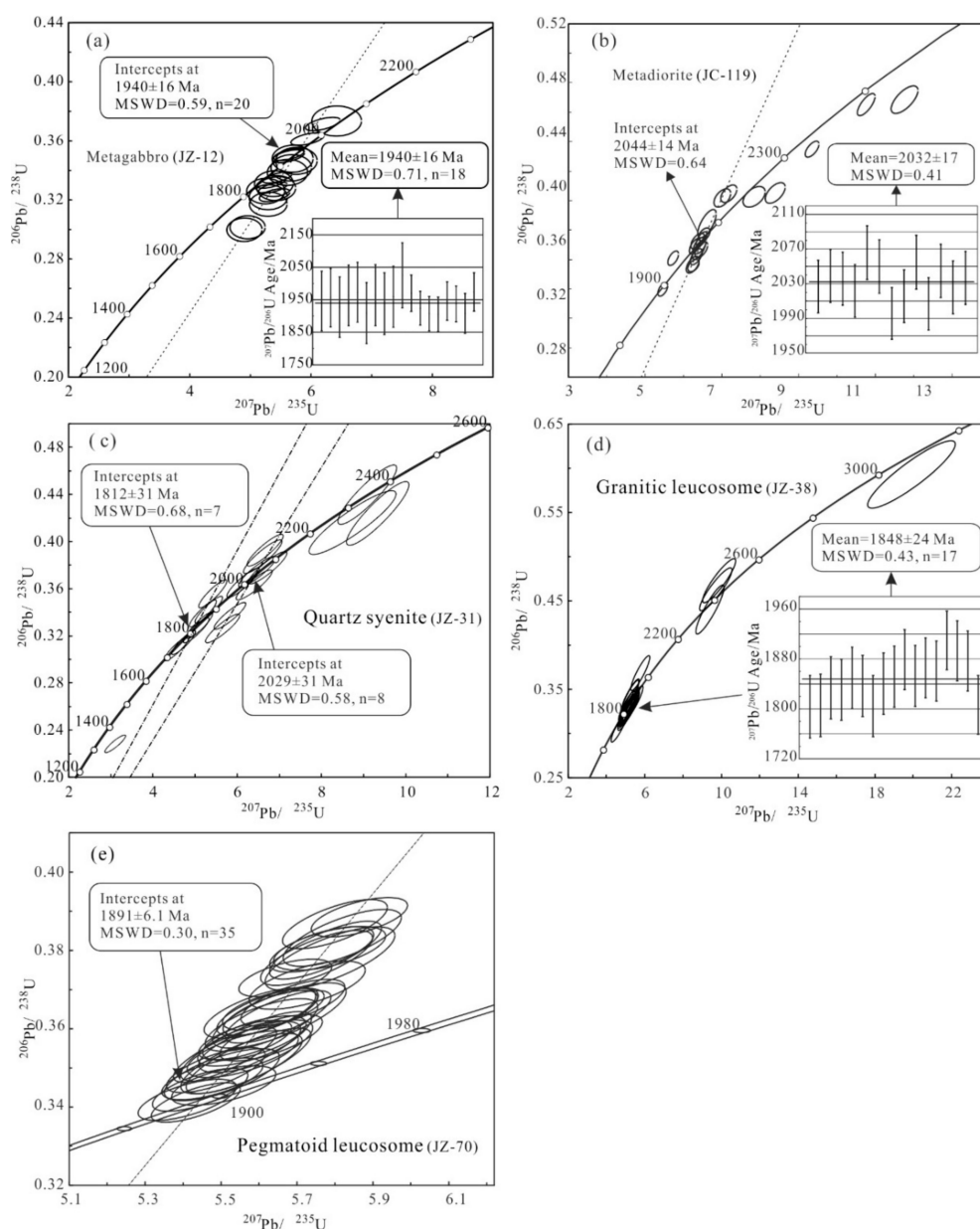


Figure 8. Concordia diagrams for zircon LA-ICPMS U–Pb analyses. (a) Metagabbro sample JZ-12; (b) metadiorite sample JC-119; (c) quartz syenite sample JZ-31; (d) granitic leucosome sample JZ-38; (e) pegmatoid leucosome sample JZ-70.

Thirteen zircons were analyzed for Lu–Hf isotopes from sample JZ-12. The $^{176}\text{Hf}/^{177}\text{Hf}$ ratios of thirteen spots are in the range of 0.281567 to 0.281638, which convert to $\epsilon\text{Hf}(t)$ values of -0.16 – 2.58 (Figure 9a), and two-stage Hf isotope depleted mantle model ages ($T_{\text{DM}2}$) of 2.58 to 2.41 Ga.

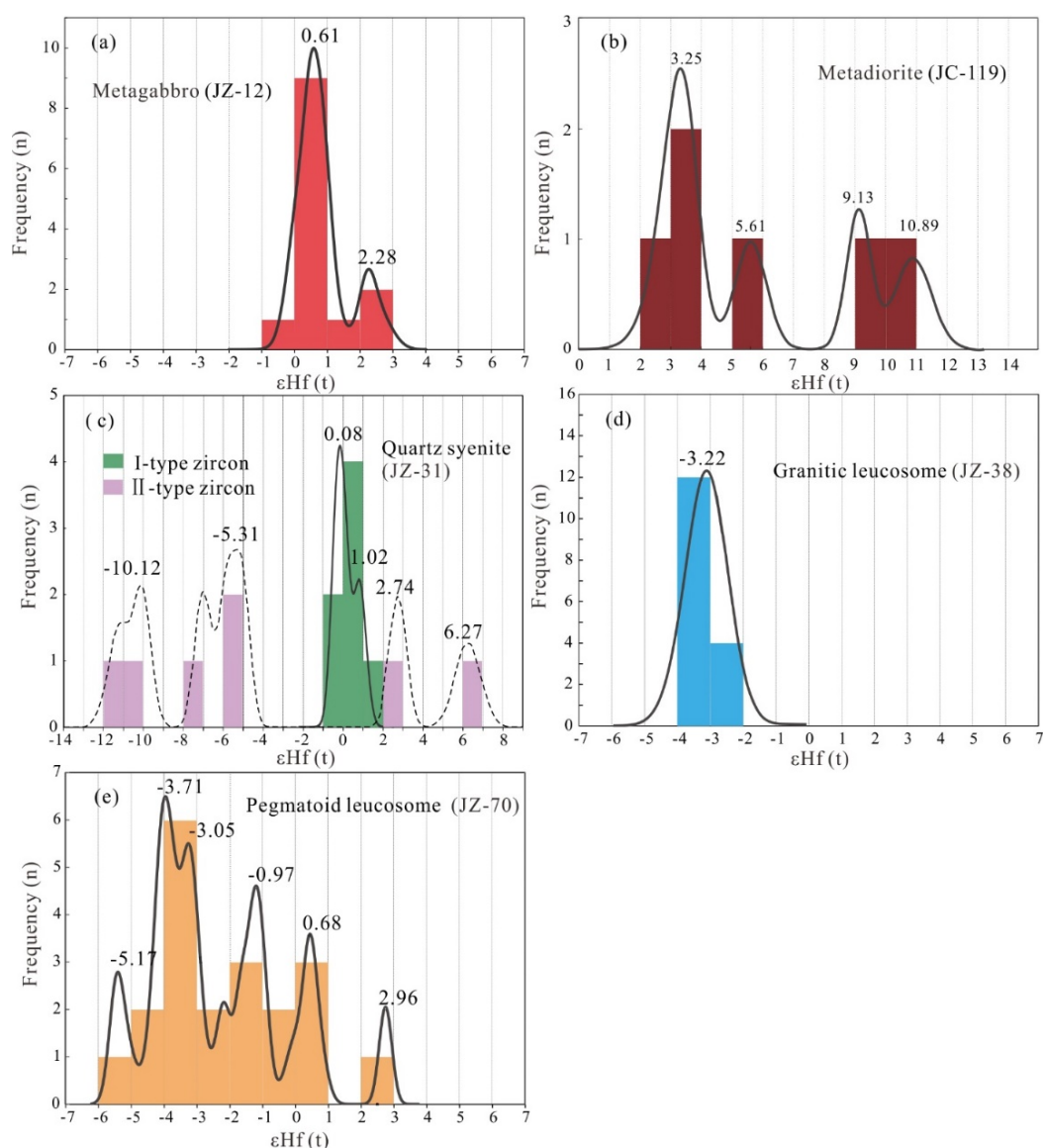


Figure 9. Probability plots of zircon $\epsilon\text{Hf}(t)$ values. (a) Metagabbro sample JZ-12; (b) metadiorite sample JC-119; (c) quartz syenite sample JZ-31; (d) granitic leucosome sample JZ-38; (e) pegmatoid leucosome sample JZ-70.

5.2.2. Metadiorite (JC-119)

Zircons in the metadiorite (JC-119) mainly have bright CL intensity and oscillatory zoning (Figure 7b) with Th/U ratios of 0.1–1.79. Among these, thirteen spots yield a concordia upper intercept age of 2044 ± 14 Ma (MSWD = 0.61) (Figure 8b), which is concordant with the weighted mean $^{207}\text{Pb}/^{206}\text{Pb}$ ages of 2032 ± 17 Ma (MSWD = 0.41). Five spots domains have $^{207}\text{Pb}/^{206}\text{Pb}$ ages of 2236 Ma to 2658 Ma. Meanwhile, spot #9 and #24 show weakly luminescent and lacking discernible internal structure with Th/U ratios of 0.06–0.09. They have $^{207}\text{Pb}/^{206}\text{Pb}$ ages of 1890 Ma and 1880 Ma, respectively.

Nine zircons were analyzed for Lu–Hf isotopes from sample JC-119. Six zircon spots, which define the concordia upper intercept age of 2044 ± 14 Ma, show $^{176}\text{Hf}/^{177}\text{Hf}$ and $\epsilon\text{Hf}(t)$ values of 0.281602 to 0.281865 and 2.97 to 10.89 (Figure 9b), respectively, with $T_{\text{DM}2}$ of 1976 Ma to 2467 Ma.

5.2.3. Quartz Syenite (JZ-31)

In this sample, two distinct groups of zircons (I-type and II-type) were identified by using CL images (Figure 7c). The I-type zircons commonly have core-rim structures (such as #2, #10, #11, #16 and #21), and their cores have bright CL intensity and oscillatory zoning with Th/U ratios of 0.25–0.60. Meanwhile, their rims appear weakly luminescent and show no discernible internal structure. Except for three analyses (#4, #33 and #34) with $^{207}\text{Pb}/^{206}\text{Pb}$ ages of 2344 Ma to 2452 Ma, the other eight analytical spots of the core of I-type zircons yield a concordia upper intercept age of 2029 ± 31 Ma (MSWD = 0.58) (Figure 8c). The dark rim of the I-type zircon is too narrow (<10 μm) to analyze. The II-type zircons (such as #13 and #18) appear weakly luminescent and unzoned with Th/U ratios of 0.02–0.09 (Figure 7c). Except for spot #8 with $^{207}\text{Pb}/^{206}\text{Pb}$ ages of 1602 Ma, the other seven analytical spots of II-type zircons yield a concordia upper intercept age of 1812 ± 31 Ma (MSWD = 0.68) (Figure 8c).

The $^{176}\text{Hf}/^{177}\text{Hf}$ ratios of seven spots from the I-type zircon domains are in the range of 0.281523 to 0.281576, which converts to homogenous $\epsilon\text{Hf}(t)$ values of -0.15 to 1.21 (Figure 9c), and $T_{\text{DM}2}$ of 2.65 to 2.56 Ga. The $^{176}\text{Hf}/^{177}\text{Hf}$ ratios of seven spots from the II-type zircon domain are in the range of 0.281413 to 0.281861, which converts to variations $\epsilon\text{Hf}(t)$ values of -11.21 to 6.24 (Figure 9c), and $T_{\text{DM}2}$ of 2.08 to 3.16 Ga.

5.2.4. Granitic Leucosome (JZ-38)

Zircons in the granitic leucosome (JZ-38) mainly occur as oval to spherical-shape, new and simple crystals. They exhibit dark CL intensities with weak oscillatory zoning (Figure 7d) and low Th/U value (0.06–0.10). Seventeen analytical spots yield a weighted mean $^{207}\text{Pb}/^{206}\text{U}$ age of 1848 ± 24 Ma (MSWD = 0.43) (Figure 8d). Spots #2, #3, #6 and #34 show oscillatory zoning in CL images with Th/U values of 0.33 to 0.57. They have $^{207}\text{Pb}/^{206}\text{Pb}$ ages of 2355 Ma to 3137 Ma.

The $^{176}\text{Hf}/^{177}\text{Hf}$ ratios of the sixteen anatectic zircons, which define the weighted mean age of 1848 Ma, are in the range of 0.281517 to 0.281562, which converts to $\epsilon\text{Hf}(t)$ values of -2.66 to -2.62 (Figure 9d), and $T_{\text{DM}2}$ of 2.74 to 2.43 Ga.

5.2.5. Pegmatoid Leucosome (JZ-70)

Zircons in this sample are brown and non-transparent. Most of them are oval-shape with grain diameter of 300–600 μm and length-width ratios of 1:1–2:1. They have dark CL intensity, weak oscillatory zoning and no inherited cores or resorption (Figure 7e), with Th/U ratios of 0.07–0.23. Thirty-five analytical spots yield a concordia upper intercept age of 1891 ± 6.1 Ma (MSWD = 0.59) (Figure 8e).

The $^{176}\text{Hf}/^{177}\text{Hf}$ ratios of the twenty zircons are in the range of 0.281448–0.281691, and have variable $\epsilon\text{Hf}(t)$ values of -5.25 – 2.96 (Figure 9e) and $T_{\text{DM}2}$ of 2.86–2.34 Ga.

6. Discussion

6.1. Formation Age

In recent years, large numbers of Paleoproterozoic zircon U–Pb age data in the LS area have been reported in literatures. Yang [52] reported four 2500–2455 Ma old pegmatoid alaskites in the Baishiquan. Yan et al. [34] reported primarily detrital zircon U–Pb ages of 2.13–2.03 Ga and metamorphic ages of 1899 Ma, 1884 Ma, 1812 Ma, 1803 Ma from data provided by the Jinchuan Continental Scientific Drilling Core. Gong [53] obtained plausible magmatic ages of 2032 Ma, 2059 Ma, 2040 Ma, 2329 Ma, 2034 Ma, 2164 Ma, 2029 Ma, 2028 Ma and metamorphic ages of 1927 Ma, 1912 Ma, 1927 Ma, 1929 Ma, 1851 Ma, 1856 Ma, 1955 Ma from metamorphic plutonic rocks, metasedimentary rocks and amphibolites in the LS area. Two upper concordia intercept zircon ages of 2015 Ma and 1914 Ma were obtained for the granitoid gneiss and trondhjemite in the LS area, respectively, and were interpreted to reflect their emplacement age [26,27].

In this study, zircons from the metagabbro, metadiorite and quartz syenite can be divided in two groups. One group (the zircons from JZ-12, majority zircons from JC-119 and I-type zircons from JZ-31) have high Th/U ratio values (0.1–1.79), as well as bright intensity and oscillatory zoning in the CL images. These are all features indicative of a magmatic origin [54], which suggests that their crystallization ages represent the magmatic emplacement age of the rocks or the ages of captured or inherited zircons. Hence, the concordia upper intercept ages of 1940 ± 16 Ma ($n = 20$, MSWD = 0.59; JZ-12), 2044 ± 14 Ma ($n = 13$, MSWD = 0.61; JC-119) and 2029 ± 31 Ma ($n = 8$, MSWD = 0.58; I-type zircons from JZ-31) are mostly likely taken to represent the magmatic emplacement age of metagabbro, metadiorite and quartz syenite, respectively. Five analyses from the JC-119 and three analyses from JZ-31 have $^{207}\text{Pb}/^{206}\text{Pb}$ ages of 2236 Ma to 2658 Ma and 2344 Ma to 2452 Ma, which are much older than the emplacement ages of metadiorite and quartz syenite. Hence, these zircons are captured or inherited zircons. The second zircon group (the spots #9 and #24 from JC-119 and II-type zircons from JZ-31) have low Th/U ratio values (0.02–0.09), as well as weakly luminescent and lacking discernible internal structure in the CL images, which suggests that their ages most likely represent the timing of metamorphism. Moreover, the ages of 1890 Ma (spot #9 from JC-119), 1880 Ma (spot #24 from JC-119) and 1812 ± 31 Ma ($n = 8$, MSWD = 0.68; II-type zircons from JZ-31) is consistent with the metamorphic ages in the LS area in previous research [34,53].

Majority zircons from the granitic leucosome (JZ-38) and zircons from the pegmatite leucosome (JZ-70) occur as oval to spherical-shape, with anhedral or, less commonly, euhedral sharp crystal edges. They have homogeneous or weak oscillatory zoning with relatively low Th/U ratio (granitic leucosome: 0.04–0.11, pegmatoid leucosome: 0.07–0.23). These are consistent with those of zircons from leucosome in migmatite [55,56]. Hence, the zircon U–Pb ages of 1848 ± 24 Ma (MSWD = 0.48) and 1891 ± 6.1 Ma (MSWD = 0.59) are interpreted to reflect the formation age for the granitic leucosome and pegmatoid leucosome, and directly date the high-grade metamorphism and crustal anataxis in the LS area. In addition, five zircons from the JZ-38 (spot #2, #3, #6 and #34) have high Th/U ratio values (0.33–0.57) and oscillatory zoning in the CL images. They have $^{207}\text{Pb}/^{206}\text{Pb}$ ages of 2355–3137 Ma, which are much older than the formation age of granitic leucosome. Hence, these five zircons are most likely captured or inherited igneous zircons.

Combined with previous studies [26,27,34,52,53], lead to the geochronological framework of the Paleoproterozoic in the LS area: (1) three magmatic events occurred at 2.5–2.45 Ga, ~2.1–2.0 Ga and ~1.95–1.91; and (2) three periods of major regional metamorphism/anataxis events occurred during the late Paleoproterozoic at ~1.93–1.89 Ga, ~1.86–1.84 Ga and ~1.81 Ga. The ~2.1–2.0 Ga magmatic event and ~1.93–1.89 Ga metamorphism/anataxis event are more intense than others.

6.2. Crustal Growth of the LS Area from Neoproterozoic to Paleoproterozoic

The integration of U–Pb dating and Hf isotope tracer information contained within zircons has been widely used to decipher the evolution of the continental crust [57–60]. In this study, we chose the spots from the magmatic zircon domains to draw the $\epsilon\text{Hf}(t)$ -age(Ma) diagram (Figure 10). As shown in Figure 10, most spots define a crustal evolutionary line that intersects the depleted mantle line at ~2.9–2.5 Ga, which represents a significant period of crustal growth in the LS area. Hence, we suggest that the LS area had a crustal growth period similar to other parts of the NCC and most ancient cratons worldwide (~2.9–2.7 Ga and ~2.6–2.5 Ga) [2,61–63]. At ~2.1 Ga, the $\epsilon\text{Hf}(t)$ values of zircons are significantly increased and three spots fall on the depleted mantle evolutionary line. These suggest a significant juvenile crustal growth event in this period. Furthermore, some spots define a crustal evolutionary line that intersects the depleted mantle line at about 2.2–2.0 Ga (Figure 10). Hence, the secondary crustal growth events could have taken place at about 2.2–2.0 Ga. In addition, there are several zircons with $\epsilon\text{Hf}(t)$ values lower than the 2.9 Ga line, indicating possible existence of older components in the deep crust. Furthermore, the line defined by four of them intersects the mantle line at ~3.2 Ga and one of them has high $\epsilon\text{Hf}(t)$ values close to the depleted mantle evolutionary line. Hence, it can be concluded that some Paleoproterozoic components may be present in the area, although

more work is needed to verify this conclusion. In summary, two main crustal growth events in the LS area happened at ~2.9–2.5 Ga and ~2.2–2.0 Ga.

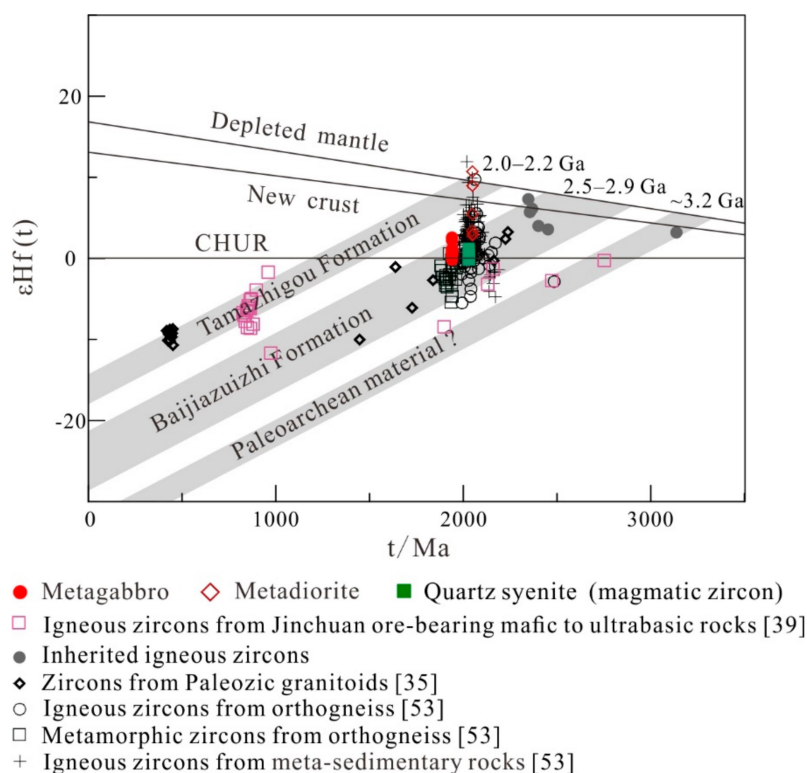


Figure 10. Zircon $\epsilon\text{Hf}(t)$ -age(Ma) diagrams. Depleted mantle: $^{176}\text{Lu}/^{177}\text{Hf} = 0.0384$ [64]; CHUR: $^{176}\text{Lu}/^{177}\text{Hf} = 0.0332$ [65].

The LS Group is the basement rocks in the LS area. However, its formation age remains a topic of debate. Based on the earlier isotopic data, including Rb-Sr, K-Ar, Sm-Nd, Tang [66] indicated that the oldest formation age of the LS Group is Mesoarchean. However, based on the zircon U-Pb method, Xiu et al. [26,27] proposed that the LS Group was mainly formed during the Paleoproterozoic, because no Archean zircons have been found in the LS area. According to the U-Pb-Hf isotopes in zircons from two Paleozoic granitoids, Zeng et al. [35] suggested that the Paleoproterozoic is one of the important periods for the formation of the LS Group. In addition, Tung et al. [32] supposed that the lithification age of the LS Group should be younger than Paleoproterozoic by using SHRIMP technique for detrital zircons. In the present studies, abundant igneous rocks widely intruded into the Baijiazuzhi Formation and Tamazigou Formation of the LS Group. The 2500~2455 Ma old pegmatoid alaskites, which was dated by using zircon LA-ICP-MS U-Pb method [52], is the oldest igneous rock yet found in the Baijiazuzhi Formation. Meanwhile, the 1940 Ma old metagabbro is the oldest igneous rock yet found in the Tamazigou Formation. Hence, the deposition age of the Baijiazuzhi Formation and Tamazigou Formation are earlier than 2.5 Ga and 1.94 Ga, respectively. In combination with the conclusions in the preceding paragraph, we concluded that the Baijiazuzhi Formation and Tamazigou Formation of the LS Group were formed at ~2.9–2.5 Ga and ~2.2–2.0 Ga, respectively.

6.3. Petrogenetic Implications

6.3.1. Meta-Mafic Rocks

The metagabbro is characterized by relatively low zircon $\epsilon\text{Hf}(t)$ value (−0.15–1.21), enrichment of LREE and LILE and weak depletion in Nb, Ta and Ti, indicating that the rock derived from an

enriched mantle source and/or underwent crustal contamination during ascent within continental crust [67]. The samples of the metagabbro have low SiO₂ and REEs content, high MgO, Mg#, Ni and Cr content and have no correlation in the diagrams of Nb/La vs. SiO₂ (Supplementary Materials Figure S1), indicating that the rocks did not experience substantial crustal contamination during magmatic evolution [68–70]. This interpretation is also supported by the following lines of evidence: (1) The metagabbro has similar zircon $\epsilon\text{Hf}(t)$ values and common features of most major and trace elements (Figures 4 and 5a,b); (2) Lu/Yb ratios of our samples generally range from 0.14–0.15, which is consistent with that of mantle-derived magmas (0.14–0.15) and is lower than that of continental crust (0.16–0.18) [71]; and (3) absence of ancient captured zircons does not support significant crustal contamination [72]. Hence, the metagabbro most likely derived from an enriched mantle source.

Compared with metagabbro, the metadiorite have high SiO₂ content, low MgO, Ni, Cr content and Mg# value, implying that the rocks experienced crustal contamination during magmatic evolution. Moreover, the wide range of zircon Hf compositions, indicating mixing between two magmatic end-members. The positive $\epsilon\text{Hf}(t)$ values are close to the value of depleted mantle at that time, suggesting one end-member deriving from a depleted mantle. The low zircon $\epsilon\text{Hf}(t)$ value and presence of ancient captured zircons suggests the contribution of ancient continental crust in magma genesis. Hence, the metadiorite deriving from a depleted mantle, and experienced crustal contamination during magmatic evolution. A detailed simulation using zircon Hf isotopes indicates that the ratio of depleted mantle derived magma to ancient crustal derived magma in the parental magmas of the metadiorite is 9:1. In the rough mixing calculation, the $\epsilon\text{Hf}(t)$ value of the depleted mantle derived magma, ancient crustal derived magma and parental magmas of the granodiorite porphyry are 10.89 (the maximum measured $\epsilon\text{Hf}(t)$ value), 2.97 (the minimum measured $\epsilon\text{Hf}(t)$ value) and 5.85 (the average measured $\epsilon\text{Hf}(t)$ value), respectively. The assumed Hf contents of the depleted mantle derived magma and ancient crustal derived magma are 0.309 $\mu\text{g/g}$ and 4.0 $\mu\text{g/g}$ within the depleted mantle [73] and the average of crust from the North China Craton [74], respectively.

6.3.2. Quartz Syenite

Granites are commonly divided into I-, S-, M- and A-types depending on their origin. The surrounding rock (marble) of the quartz syenite has no obvious alteration by this magmatic event. In addition, the quartz syenite is composed of massive felsic minerals and rare water-bearing minerals. Furthermore, due to crystallization of anhydrous minerals phase at an early stage, fractional crystallization of a primary hydrous I-type or S-type granitic magma would lead to higher water content in the magma at a late stage. However, the quartz syenite in this study is characterized by development of biotite filling in quartz and feldspar (Figure 3e), implying that the biotite formed in the late stage of magmatic crystallization in an anhydrous or water-poor magma [75,76]. Hence, the above petrological features imply that the parent magma of the quartz syenite had low volatile content consistent with anhydrous of A-type granites.

According to the Watson and Harrison [77] calibration method, the T_{Zr} of the quartz syenite is in the range of 921–1067 °C, except one. Hence, the quartz syenite clearly have high crystallization temperatures consistent with A-type granites (>900 °C, [78,79]), which is significantly higher than that of I- and S-type granite. In addition, with the rise of the degree of crystallization differentiation, P₂O₅ content in S-type granite increases, accompanied by a decrease in Th and Y [80]. However, the P₂O₅ content of the quartz syenite has a negative correlation with SiO₂ and positive correlation with Th and Y (Supplementary Materials Figure S2), indicating the quartz syenite is not an S-type granite. Moreover, the samples display high contents of SiO₂, total alkali (K₂O + Na₂O) and REE, features consistent with A-type granite [81–83], and the composition of these samples fall into the field of A-type granite in the discrimination diagrams of granites introduced by Whalen et al. [81] (Figure 11). As a result, the petrography and geochemical characteristics strongly suggest an A-type affinity for the quartz syenite. A-type granite has been further divided into A1 and A2 on the basis of

chemistry by Eby [84]. The samples plot into the A1-type granites field in the Y-3G-Nb and Y/Nb-Yb-Ta diagrams (Figure 12), indicating that the quartz syenite should be classified as A1-type granite.

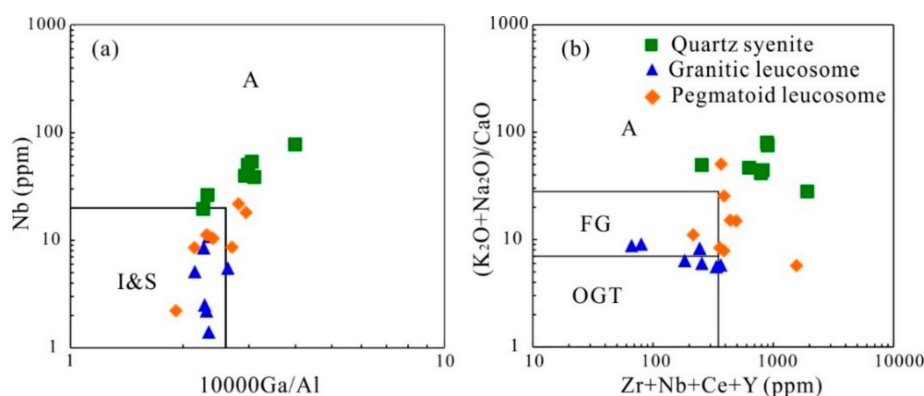


Figure 11. Discrimination of granitoids genetic types (modified from [81]). FG = fractionated M-, I- and S-type granites; OGT—unfractionated M-, I- and S-type granites.

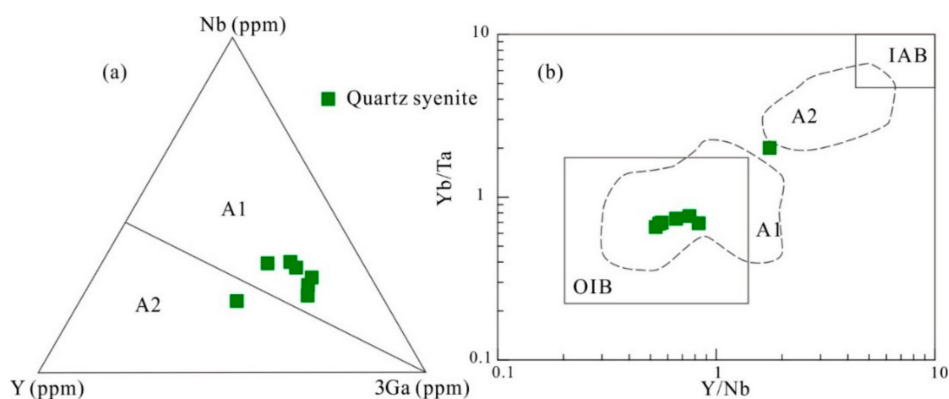


Figure 12. Nb-Y-Ce (a) and Yb/Ta-Y/Nb diagrams (b) for the QS (modified from [84]). OIB = oceanic island basalt; IAB = island arc basalt. Fields with dashed lines represent A1- and A2-type granites of Eby [84].

A variety of petrogenetic models have been proposed for the origin of A-type granite, such as fractional crystallization of mantle derived basaltic magma, mixing of mantle-derived and crust-derived magmas, and partial melting of crustal materials [85,86]. Based on experimental and geochemical work, Clemens et al. [87] and King et al. [88] proposed that extensive fractional crystallization of mantle derived basaltic magma is unlikely to be the petrogenetic model for A-type granite, because A-type granite formed at temperatures higher than their calc-alkaline counterparts. Meanwhile, the lower Mg#, MgO, TFe₂O₃, CaO, Na₂O and Cr contents and relatively higher SiO₂ and K₂O contents are totally different from mantle-derived magmas. Moreover, the rocks have zircon ϵ Hf(t) values with a narrow range (−0.15–1.21) and no coeval mantle-related mafic enclaves. Hence, the contribution of mantle materials must have been minor or absent. As a consequence, partial melting of crustal rocks is most likely the origin of the quartz syenite. The T_{DM2} of 2.65 to 2.56 Ga suggest that the source material of the quartz syenite was derived from reworked Mesoproterozoic components.

The metamorphic zircons show large variations in ¹⁷⁶Hf/¹⁷⁷Hf ratios (from 0.281413 to 0.281861) than that of the protolith igneous zircons. It indicates that the crystallization of metamorphic zircons from externally derived Zr-bearing melt occurred during metamorphism/anatexis event in an open system [89,90].

6.3.3. Leucosome

The granitic leucosome and pegmatoid leucosome in this study appear as leucosome in protolith, do not contain special minerals (such as hafnium zircon, beryl or columbite-tantalite), and have no whole-rock REE tetrad effect. These indicate that the granitic leucosome and pegmatoid leucosome formed from initial melt during migmatization, rather than last residual melt after crystal fractionation [90]. It is reinforced by the zircons from the granitic leucosome and pegmatoid leucosome, which have the feature of zircon from leucosomes in migmatites. In addition, outwards from the pegmatoid leucosome, the proportion of leucosome in the schlieren migmatite continues to decline, and then transfer to plagioclase amphibolite (Figure 3h). The transition is an in situ melting process that records progressive disaggregation of the rock [91].

The homogenous low $\epsilon\text{Hf}(t)$ values (-2.66 to -2.62) and old T_{DM2} (2.74 to 2.43 Ga) of zircons in granitic leucosome imply a single source from Mesoarchean to Neoproterozoic components. However, the zircons from the pegmatoid leucosome have variations in $\epsilon\text{Hf}(t)$ values (-5.25 to 2.96). The positive $\epsilon\text{Hf}(t)$ values for the pegmatoid leucosome can be interpreted as deriving from mantle magma or juvenile crust [35,89]. Since initial melt during migmatization is the formation mechanism of the pegmatoid leucosome, the source region of pegmatoid leucosome should be near the current position. However, we have found no ~ 1890 Ma ultramafic and/or mafic igneous rocks in the Jinchuan mining area or even the LS area. In addition, the samples of pegmatoid leucosome have low Mg# values and high SiO_2 content, which fall into the field of pure crustal melts (Supplementary Materials Figure S3). Therefore, partial melting of juvenile and ancient crustal sources is considered the most likely model for the petrogenesis of the pegmatoid leucosome.

6.4. Model for Tectonic Evolution of LS Area

Zhai and Peng [92] and Zhai [93] proposed that the NCC experienced intracratonic orogenesis events during ~ 2.3 – 1.95 Ga. In the Bayanwulashan area, eastern Alxa Block, Dan et al. [22] reported that the ~ 2.34 Ga mafic rocks are geochemically similar to the basaltic rocks formed within continental rifts. In the LS area, three middle Paleoproterozoic granites, 2233 Ma [94], 2103 Ma and 2072 Ma [95], have been reported by using the zircon U–Pb method. These granites have all been interpreted as having formed in an intraplate-extensional post-collisional setting [94,95]. In this study, LA-ICP-MS zircon U–Pb data constrains the emplacement age of the A1-type quartz syenite at 2029 Ma and metadiorite at 2032 Ma. On the one hand, it is commonly accepted that A-type granites are formed in extensional tectonic environments [84,96,97]. Furthermore, A1-type and A2-type have different tectonic settings, with the former emplaced in an anorogenic intraplate setting [82]. On the other hand, based on the tectonic discrimination diagrams introduced by Pearce and Norry [98], the composition of metadiorite samples fall in the within plate basalts field (Figure 13). Moreover, the sample of metadiorite have Nb/Zr and Th/Nb from 0.067 to 0.068 and 0.23 to 0.24, respectively, similar to continental rift basalts (Nb/Zr > 0.04 and Th/Nb = 0.11–0.27 [99]). Thus, during the middle Paleoproterozoic, the LS area was in an intraplate extensional setting (Figure 14a). The extensional setting induced mantle magma upwelling, which directly lead to mafic magmatism and provided thermal flux to melt the overlying crust and form the acidic magmatism at ~ 2.0 Ga. Since the protolith of the graphite marble in the Tamazigou Formation was formed in a stable shallow sea environment [32,66]. Our determination in Section 6.2 above, which the Tamazigou Formation formed during ~ 2.2 – 2.0 Ga is reasonable.

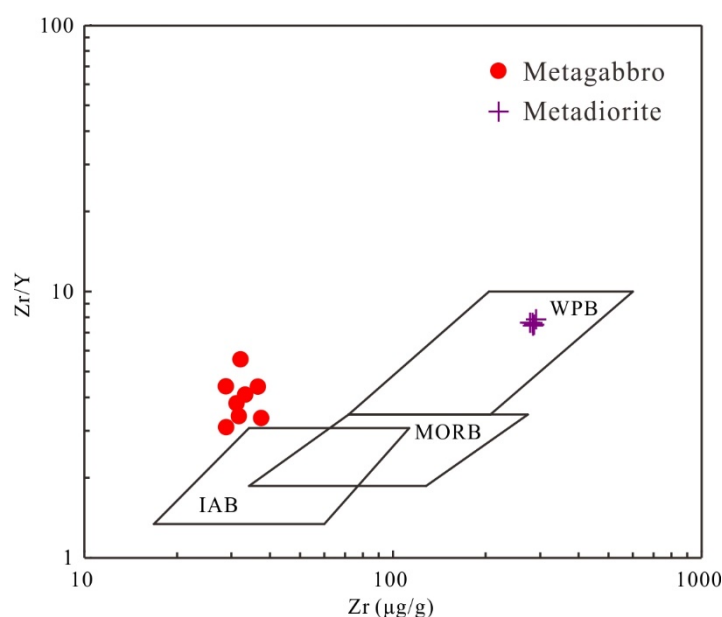


Figure 13. Zr/Y-Zr diagram for the meta-mafic rocks [98]. MORB = mid-ocean ridge basalt; IAB = island arc basalt; WPB = within plate basalt.

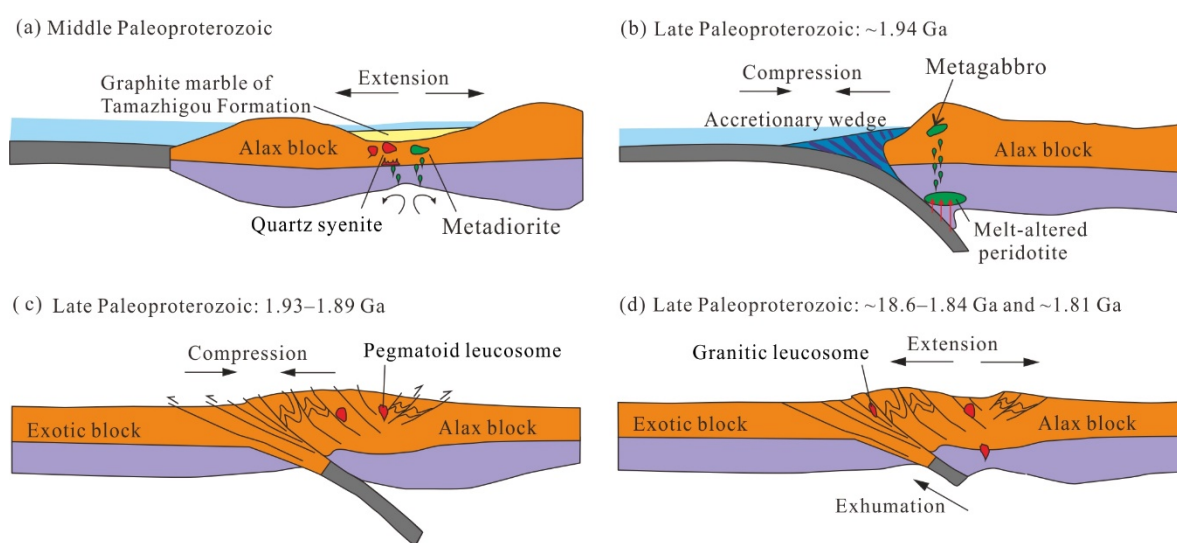


Figure 14. Tectonic evolution of the southwest margin of the NCC in four stages in middle to late Paleoproterozoic. (a) intraplate extensional setting in the middle Paleoproterozoic; (b) convergent setting at ~1.94 Ga; (c) continental subduction at 1.93–1.89 Ga; (d) exhumation at ~1.86–1.84 Ga and ~1.81 Ga.

The emplacement age of the metagabbro is determined at 1940 Ma. The samples of the metagabbro show low Nb/La (0.22–0.48) and Hf/Ta (7–10, except one sample) ratios, which differ from within-plate basalts and ocean-ridge basalt (Nb/La > 1 and Hf/Ta < 5). Meanwhile, they have high Th/Nb (0.7–1.1) and Th/Yb (1.4–2.1) ratios, and low Hf/Th (0.6–0.9) and Ti/V (10–12) ratios, which are similar to arc basalt (Th/Nb > 0.07, Th/Yb > 0.1, Hf/Th < 8 and Ti/V < 20) [100,101]. In addition, they have high Zr/Y (3.10–5.58) and Ta/Yb (0.11–0.28) ratios, similar to calc-alkaline basalts from continental-margin arcs (Zr/Y > 3 and Ta/Yb > 0.1), and clearly higher than those of island arc basalt and calc-alkaline basalt from island arcs [100]. Thus, the metagabbro is geochemically akin to the basaltic rocks formed

in continental-margin arc environments. The formation age of the metagabbro is consistent with the timing of the assembly of the Western Block at 1.95–1.90 Ga [1,9–13]. Therefore, we conclude the LS area was in a convergent setting at ca.1.94 Ga after a period of extensional intraplate evolution in the middle Paleoproterozoic (Figure 14b). The enriched mantle, which provided materials for magma genesis of the metagabbro, was most likely generated by reaction of subcontinental lithospheric mantle (SCLM) peridotite with felsic melts from partial melting of the subducted oceanic crust during this time in this subduction zone.

Generally, partial melting is considered to be a significant process in the evolution of collisional orogen [102–105]. The anatexis events generated by continental subduction and exhumation are reported in the Dabie-Sulu and western Norway [104,105]. As mentioned above, the ~1.93–1.89 Ga, ~1.86–1.84 Ga and ~1.81 Ga anatexis/metamorphic events are well developed in the LS area, especially the oldest one. The ~1.93–1.89 Ga anatexis/metamorphic event is slightly younger than the 1940 Ma old continental-margin arc basalt (metagabbro). Hence, the initial age of continental collision should be between 1.94–1.93 Ga, and the 1.93–1.89 Ga anatexis/metamorphic events can reasonably be expected to record the timing of partial melting and migmatization that resulted from continental subduction (Figure 14c). Since 1.93–1.81 Ga old ophiolite and arc-derived magmas rocks have not been found in the LS area, the ~1.86–1.84 Ga and ~1.81 Ga anatexis/metamorphic event most likely does not represent another continental collision event. Due to a multistage exhumation of the thickened crust, multiple partial melting often occurs in orogenic belts, such as the Himalayan Orogen and the Qinling Orogen [106–108]. Thus, the ~1.86–1.84 Ga and ~1.81 Ga anatexis/metamorphic events in the LS area were most likely recorded two decompression melting during exhumation (Figure 14d). In summary, the research area experienced continental collision at 1.94–1.93 Ga, and anatexis/metamorphic events by causing continental subduction at 1.93–1.89 Ga and exhumation at ~1.86–1.84 Ga and ~1.81 Ga.

Many continental fragments, such as Laurentia, Baltica, Amazonia and India, recorded a late Paleoproterozoic orogenic event, which is considered to correlate with the assembly of Columbia [1,3,4,109–111]. In the LS area, multi-stage regional metamorphism/anatexis events occurred during the late Paleoproterozoic. This indicated that the LS area were most likely involved in this late Paleoproterozoic assembly process.

6.5. Implications for Comparison to the Other Parts of the NCC

To identify the tectonic affinity of the Alxa block, we compare the Neoproterozoic to Paleoproterozoic geochronological frameworks of the LS area with that of the Khondalite Belt and the Yinshan Block. Two Paleoproterozoic magmatic events at ~2.06–2.0 Ga and ~1.97–1.9 Ga [25,112–115], and two Paleoproterozoic metamorphism events at ~1.93–1.88 Ga and ~1.85–1.81 [11,13,25,112,116–120] have been well documented in the Khondalite Belt. As discussed at Section 6.1, the ~2.1–2.0 Ga and ~1.95–1.91 Ga magmatism events and ~1.93–1.89 Ga, ~1.86–1.84 Ga and ~1.81 Ga metamorphism events are also widespread in the LS area, indicating the similar sequence of magmatic metamorphism events to those of the Khondalite Belt. Moreover, the ~1.95 Ga mafic rocks in Daqingshan area are low in K_2O and P_2O_5 , limited enriched in LREE ($La_N/Yb_N = 3.1–3.8$) and enrichment of LILE with negative Ta and Nb [114], which is highly similar to those of the 1940 Ma metagabbro in this paper. To the contrary, the geochronological framework of the LS area is totally different from that of the Yinshan Block, which experienced an intense magmatic event in the late Neoproterozoic (~2.57–2.5 Ga), and underwent a two-stage metamorphic event at ~2.50 Ga and ~2.48 Ga [121–124].

Moreover, the Khondalite Belt is a continent-continent collisional belt, which the Yinshan Block collided with the Ordos Block to form the Western Block at ~1.95–1.90 [1,25,120]. As discussed in Section 6.5, the LS area went through two stages-setting during ~1.94–1.89 Ga, continental-margin arc setting and continental collision setting, and the initial age of continental collision occurred at 1.94–1.93 Ga. Hence, the Paleoproterozoic tectonic evolution of the LS area is also similar to that of the Khondalite Belt.

As argued above, we suggest that the Alxa Block is most likely the western extension of the Khondalite Belt rather than the Yinshan Block.

7. Conclusions

- A. In the LS area, there were three major periods of magmatism during Paleoproterozoic: ~2.5–2.45 Ga, ~2.1–2.0 Ga and ~1.95–1.91 Ga, and three major regional metamorphism/anatexis events at ~1.93–1.89 Ga, ~1.86–1.84 Ga and ~1.81 Ga, respectively.
- B. The age-Hf isotope data indicate that two main crustal growth events happened at ~2.9–2.5 Ga and ~2.2–2.0 Ga in the LS area. And the two episodes are confirmed by the depositional ages of the Baijiazuizi Formation and Tamazigou Formation of the LS Group, respectively.
- C. In the middle Paleoproterozoic, the LS area entered an intraplate extensional setting. After that, the LS area was in a strongly convergent collision environment. In the late Paleoproterozoic, the research area is experienced continental collision at 1.94–1.93 Ga, and anatectic/metamorphic events by causing continental subduction at 1.93–1.89 Ga and exhumation at ~1.86–1.84 Ga and ~1.81 Ga.
- D. The geochronological framework and tectonic evolution of the LS area show stronger affinity toward the Khondalite Belt rather than the Yinshan Block, supporting the argument that the Alxa Block is a western extension of the Khondalite Belt.

Supplementary Materials: The following are available online at <http://www.mdpi.com/2075-163X/8/9/361/s1>, Figure S1: Nb/La-SiO₂ diagram for metagabbro, Figure S2: P₂O₅-SiO₂, Y-P₂O₅ and Th-P₂O₅ diagram for quartz syenite, Figure S3: Mg#-SiO₂ diagram for pegmatoid leucosome, Table S1: Major element (%) and trace element (ppm) compositions for five rock types in the LS area, Table S2: Zircon La-ICP-MS U-Pb isotopic data and ages for five rock types in the LS area, Table S3: Zircon Hf isotopic data for five rock types in the LS area.

Author Contributions: R.Z. and J.L. conceived and designed the experiments; J.L., X.M., B.L., J.Z. and L.Y. took part in the discussion; R.Z. and R.C.B. wrote the paper.

Acknowledgments: This research was funded by the National Nature Science Foundation of China (Grants No. 41172297 and 41472301), the Project of Innovation-driven Plan in Central South University (Grant No. 2015CX008), the Jiangxi Provincial Department of Education (Grant No. GJJ170463), and the research grants from the East China University of Technology (Grant No. DHBK2017103).

Conflicts of Interest: The authors declare no conflict of interest.

References

1. Zhao, G.C.; Sun, M.; Wilde, S.A.; Li, S.Z. Late Archean to Paleoproterozoic evolution of the North China Craton: Key issues revisited. *Precambrian Res.* **2005**, *136*, 177–202. [[CrossRef](#)]
2. Zhai, M.G.; Santosh, M. The early Precambrian odyssey of the North China Craton: A synoptic overview. *Gondwana Res.* **2011**, *20*, 6–25. [[CrossRef](#)]
3. Zhao, G.C.; Wilde, S.A.; Cawood, P.A.; Lu, L.Z. Tectonothermal history of the basement rocks in the western zone of the North China Craton and its tectonic implications. *Tectonophysics* **1999**, *310*, 37–53. [[CrossRef](#)]
4. Zhao, G.C.; Sun, M.; Wilde, S.A.; Li, S.Z. Assembly, accretion and breakup of the Paleo-Mesoproterozoic Columbia Supercontinent: Records in the North China Craton. *Gondwana Res.* **2003**, *6*, 417–434. [[CrossRef](#)]
5. Kusky, T.M.; Li, J.H. Paleoproterozoic tectonic evolution of the North China Craton. *J. Asian Earth Sci.* **2003**, *22*, 383–397. [[CrossRef](#)]
6. Kusky, T.M.; Li, J.H.; Santosh, M. The Paleoproterozoic North Hebei Orogen: North China craton's collisional suture with the Columbia supercontinent. *Gondwana Res.* **2007**, *12*, 4–28. [[CrossRef](#)]
7. Liu, S.W.; Pan, Y.M.; Xie, Q.L.; Zhang, J.; Li, Q.G.; Yang, B. Geochemistry of the paleoproterozoic Nanyang granitic gneisses in the Fuping complex: Implications for the tectonic evolution of the Central Zone, North China Craton. *J. Asian Earth Sci.* **2005**, *24*, 643–658. [[CrossRef](#)]
8. Zhang, J. Th-U-Pb monazite geochronology of the Lüliang and Wutai Complexes: Constraints on the tectonothermal evolution of the Trans-North China Orogen. *Precambrian Res.* **2006**, *148*, 205–224.
9. Xia, X.P.; Sun, M.; Zhao, G.C.; Luo, Y. LA-ICP-MS U-Pb geochronology of detrital zircons from the Jining Complex, North China Craton and its tectonic significance. *Precambrian Res.* **2006**, *144*, 199–212. [[CrossRef](#)]

10. Xia, X.P.; Sun, M.; Zhao, G.C.; Wu, F.Y.; Xu, P.; Zhang, J.H.; Luo, Y. U–Pb and Hf isotopic study of detrital zircons from the Wulashan khondalites: Constraints on the evolution of the Ordos Terrane, Western Block of the North China Craton. *Earth Planet. Sci. Lett.* **2006**, *241*, 581–593. [[CrossRef](#)]
11. Santosh, M.; Tsunogae, T.; Li, J.H.; Liu, S.J. Discovery of sapphirine-bearing Mg–Al granulites in the North China Craton: Implications for Paleoproterozoic ultrahigh temperature metamorphism. *Gondwana Res.* **2007**, *11*, 263–285. [[CrossRef](#)]
12. Santosh, M.; Tsunogae, T.; Ohyama, H.; Sato, K.; Li, J.H.; Liu, S.J. Carbonic metamorphism at ultrahigh-temperatures: Evidence from North China Craton. *Earth Planet. Sci. Lett.* **2008**, *266*, 149–165. [[CrossRef](#)]
13. Santosh, M.; Wilde, S.A.; Li, J.H. Timing of Paleoproterozoic ultrahigh- temperature metamorphism in the North China Craton: Evidence from SHRIMP U–Pb zircon geochronology. *Precambrian Res.* **2007**, *159*, 178–196. [[CrossRef](#)]
14. Zhai, M. Multi-stage crustal growth and cratonization of the North China Craton. *Geosci. Front.* **2014**, *5*, 457–469. [[CrossRef](#)]
15. Yang, Q.Y.; Santosh, M.; Collins, A.S.; Teng, X.M. Microblock amalgamation in the North China Craton: Evidence from Neoproterozoic magmatic suite in the western margin of the Jiaoliao Block. *Gondwana Res.* **2015**, *31*, 96–123. [[CrossRef](#)]
16. Li, S.S.; Santosh, M.; Cen, K.; Teng, X.M.; He, X.F. Neoproterozoic convergent margin tectonics associated with microblock amalgamation in the North China Craton: Evidence from the Yishui Complex. *Gondwana Res.* **2016**, *38*, 113–131. [[CrossRef](#)]
17. Santosh, M.; Teng, X.M.; He, X.F.; Tang, L.; Yang, Q.Y. Discovery of Neoproterozoic suprasubduction zone ophiolite suite from Yishui Complex in the North China Craton. *Gondwana Res.* **2016**, *38*, 1–27. [[CrossRef](#)]
18. Geng, Y.S.; Wang, X.S.; Shen, Q.H.; Chun-Ming, W.U. Redefinition of the Alxa Group-complex (Precambrian metamorphic basement) in the Alxa area, Inner Mongolia. *Geol. China* **2006**, *33*, 138–145. (In Chinese)
19. Gong, J.H.; Zhang, J.X.; Wang, Z.Q.; Yu, S.Y.; Li, H.K.; Li, Y.S. Origin of the Alxa Block, western China: New evidence from zircon U–Pb geochronology and Hf isotopes of the Longshoushan Complex. *Gondwana Res.* **2016**, *36*, 359–375. [[CrossRef](#)]
20. Gong, J.H.; Zhang, J.X.; Yu, S.Y. The origin of Longshoushan Group and associated rocks in the Southern part of the Alxa Block: Constraint from LA-ICP-MS U–Pb zircon dating. *Acta Pet. Miner.* **2011**, *30*, 795–818. (In Chinese)
21. Zhang, J.X.; Gong, J.H.; Yu, S.Y.; Li, H.K.; Hou, K.J. Neoproterozoic–Paleoproterozoic multiple tectonothermal events in the western Alxa block, North China Craton and their geological implication: Evidence from zircon U–Pb ages and Hf isotopic composition. *Precambrian Res.* **2013**, *235*, 36–57. [[CrossRef](#)]
22. Dan, W.; Li, X.H.; Guo, J.H.; Liu, Y.; Wang, X.C. Paleoproterozoic evolution of the eastern Alxa Block, westernmost North China: Evidence from in situ zircon U–Pb dating and Hf–O isotopes. *Gondwana Res.* **2012**, *21*, 838–864. [[CrossRef](#)]
23. Zhang, J.X.; Gong, J.H. Revisiting the nature and affinity of the Alxa Block. *Acta Pet. Sin.* **2018**, *34*, 940–962. (In Chinese)
24. Santosh, M. Assembling North China Craton within the Columbia supercontinent: The role of double-sided subduction. *Precambrian Res.* **2010**, *178*, 149–167. [[CrossRef](#)]
25. Wan, Y.S.; Liu, D.Y.; Dong, C.Y.; Xu, Z.Y.; Wang, Z.J.; Wilde, S.A.; Yang, Y.H.; Liu, Z.H.; Zhou, H.Y. The Precambrian Khondalite Belt in the Daqingshan area, North China Craton: Evidence for multiple metamorphic events in the Palaeoproterozoic era. *Geol. Soc. Lond. Spec. Publ.* **2009**, *323*, 73–97. [[CrossRef](#)]
26. Xiu, Q.Y.; Lu, S.N.; Yu, H.F.; Yang, C.L. The isotopic age evidence for main Longshoushan Group contributing to Palaeoproterozoic. *Prog. Precambrian Res.* **2002**, *25*, 93–96. (In Chinese)
27. Xiu, Q.Y.; Yu, H.F.; Li, Q.; Zuo, G.C.; Li, J.W.; Cao, C.J. Discussion on the petrogenic time of Longshoushan Group, Gansu Province. *Acta Geol. Sin.-Chin. Ed.* **2004**, *78*, 366–373. (In Chinese)
28. Dong, C.Y.; Liu, D.Y.; Li, J.J.; Wang, Y.S.; Zhou, H.Y.; Li, C.D.; Yang, Y.H.; Xie, L.W. Palaeoproterozoic Khondalite Belt in the western North China Craton: New evidence from SHRIMP dating and Hf isotope composition of zircons from metamorphic rocks in the Bayan Ul-Helan Mountains area. *Chin. Sci. Bull.* **2007**, *52*, 2984–2994. [[CrossRef](#)]

29. Xu, A.D.; Jiang, X.D. Characteristics and geological significance of the Dunzigou Group of the mesoproterozoic in the western edge of the North China Platform. *J. Earth Sci. Environ.* **2003**, *25*, 27–31. (In Chinese)
30. Xiao, P.X.; You, W.F.; Cao, X.D. Redefining of the Hanmushan Group in Longshoushan, central-western Gansu Province. *Geol. Bull. China* **2011**, *30*, 1228–1232. (In Chinese)
31. Xie, C.R.; Xiao, P.X.; Yang, Z.Z.; Cao, X.D.; Hu, Y.X. Progress in the studying of the Hanmushan Group in the Longshou mountains of Gansu province. *J. Stratigr.* **2013**, *37*, 54–57. (In Chinese)
32. Tung, K.A.; Yang, H.Y.; Liu, D.Y.; Zhang, J.X.; Tseng, C.Y.; Wan, Y.S. SHRIMP U–Pb geochronology of the detrital zircons from the Longshoushan Group and its tectonic significance. *Chin. Sci. Bull.* **2007**, *52*, 1414–1425. [[CrossRef](#)]
33. Duan, J.; Li, C.S.; Qian, Z.Z.; Jiao, J.G. Geochronological and geochemical constraints on the petrogenesis and tectonic significance of Paleozoic dolerite dykes in the southern margin of Alxa Block, North China Craton. *J. Asian Earth Sci.* **2015**, *111*, 244–253. [[CrossRef](#)]
34. Yan, H.Q.; Liu, Q.F.; Tang, Z.L.; Fan, M.C.; Wang, Q.; Ren, J.M.; Fan, C.F. Structural properties of the Longshoushan Block: Constraint from LA-ICP-MS zircon U–Pb dating. *Eng. Sci.* **2015**, *17*, 59–72. (In Chinese) [[CrossRef](#)]
35. Zeng, R.Y.; Lai, J.Q.; Mao, X.C.; Li, B.; Ju, P.J.; Tao, S.L. Geochemistry, zircon U–Pb dating and Hf isotopes composition of Paleozoic granitoids in Jinchuan, NW China: Constraints on their petrogenesis, source characteristics and tectonic implication. *J. Asian Earth Sci.* **2016**, *121*, 20–33. [[CrossRef](#)]
36. Song, X.Y.; Danyushevsky, L.V.; Keays, R.R.; Chen, L.M.; Wang, Y.S.; Tian, Y.L.; Xiao, J. Structural, lithological, and geochemical constraints on the dynamic magma plumbing system of the Jinchuan Ni-Cu sulfide deposit, NW China. *Min. Depos.* **2012**, *47*, 277–297. [[CrossRef](#)]
37. Li, X.H.; Su, L.; Chung, S.L.; Li, Z.X.; Liu, Y.; Song, B.; Liu, D.Y. Formation of the Jinchuan ultramafic intrusion and the world's third largest Ni-Cu sulfide deposit: Associated with the ~825 Ma south China mantle plume? *Geochem. Geophys. Geosyst.* **2005**, *6*, 1–16. [[CrossRef](#)]
38. Zhang, M.J.; Kamo, S.L.; Li, C.S.; Hu, P.Q.; Ripley, E.M. Precise U–Pb zircon-baddeleyite age of the Jinchuan sulfide ore-bearing ultramafic intrusion, western China. *Miner. Depos.* **2010**, *45*, 3–9. [[CrossRef](#)]
39. Jiao, J.G.; Liu, H.; Duan, J.; Hao, L.U.; Luo, D.Z.; Dong, Q.I. Hf Isotope Geochemical Characteristics and Magma Sources in Jinchuan Cu-Ni Sulfide Deposit. *J. Earth Sci. Environ.* **2014**, *36*, 58–67. (In Chinese)
40. Sun, H.; Xiao, Y.L.; Gao, Y.J.; Lai, J.Q.; Hou, Z.H.; Wang, Y.Y. Fluid and melt inclusions in the Mesozoic Fangcheng basalt from North China Craton: Implications for magma evolution and fluid/melt-peridotite reaction. *Contrib. Miner. Pet.* **2013**, *165*, 885–901. [[CrossRef](#)]
41. Andersen, T. Correction of common lead in U–Pb analyses that do not report 204 Pb. *Chem. Geol.* **2002**, *192*, 59–79. [[CrossRef](#)]
42. Ludwig, K.R. *User's Manual for Isoplot 3.00, A Geochronological Toolkit for Microsoft Excel*; Berkeley Geochronological Center, Special Publication: Berkeley, CA, USA, 2003; Volume 4, pp. 1–70.
43. Woodhead, J.D.; Hergt, J.M. A preliminary appraisal of seven natural zircon reference materials for in situ Hf isotope determination. *Geostand. Geoanal. Res.* **2005**, *29*, 183–195. [[CrossRef](#)]
44. Yuan, H.L.; Gao, S.; Dai, M.N.; Zong, C.L.; Günther, D.; Fontaine, G.H.; Liu, X.M.; Diwu, C.R. Simultaneous determinations of U–Pb age, Hf isotopes and trace element compositions of zircon by excimer laser-ablation quadrupole and multiple-collector ICP-MS. *Chem. Geol.* **2008**, *247*, 100–118. [[CrossRef](#)]
45. Wu, F.Y.; Yang, Y.H.; Xie, L.W.; Yang, J.H.; Xu, P. Hf isotopic compositions of the standard zircons and baddeleyites used in U–Pb geochronology. *Chem. Geol.* **2006**, *234*, 105–126. [[CrossRef](#)]
46. Li, X.H.; Long, W.G.; Li, Q.L.; Liu, Y.; Zheng, Y.F.; Yang, Y.H.; Chamberlain, K.R.; Wan, D.F.; Guo, C.H.; Wang, X.C. Penglai Zircon Megacrysts: A Potential New Working Reference Material for Microbeam Determination of Hf-O Isotopes and U–Pb Age. *Geostand. Geoanal. Res.* **2010**, *34*, 117–134. [[CrossRef](#)]
47. Winchester, J.A.; Floyd, P.A. Geochemical discrimination of different magma series and their differentiation products using immobile elements. *Chem. Geol.* **1977**, *20*, 325–343. [[CrossRef](#)]
48. Miyashiro, A. Volcanic rock series in island arcs and active continental margins. *Am. J. Sci.* **1974**, *274*, 321–355. [[CrossRef](#)]
49. Frost, B.R.; Barnes, C.G.; Collins, W.J.; Arculus, R.J.; Ellis, D.J.; Frost, C.D. A geochemical classification for granitic rocks. *J. Pet.* **2001**, *42*, 2033–2048. [[CrossRef](#)]

50. Maniar, P.D.; Piccoli, P.M. Tectonic discrimination of granitoids. *Geol. Soci. Am. Bull.* **1989**, *101*, 635–643. [[CrossRef](#)]
51. Sun, S.S.; McDonough, W.F. Chemical and isotopic systematics of oceanic basalts: Implications for mantle composition and processes. *Geol. Soc. Lond. Spec. Publ.* **1989**, *42*, 313–345. [[CrossRef](#)]
52. Yang, C.S. Pegmatoidal Alaskite in Hongshiquan Area, Gansu Province. Master's Thesis, East China University of Technology, Shanghai, China, 2017.
53. Gong, J.H. Compositions, Characteristics, Chronological Framework and Origin of Early-Precambrian Metamorphic Basement in Western Alxa Block. Ph.D. Thesis, Institute of Geology and Geophysics, Chinese Academy of Sciences, Beijing, China, 2013. (In Chinese)
54. Hoskin, P.W.; Schaltegger, U. The composition of zircon and igneous and metamorphic petrogenesis. *Rev. Miner. Geochem.* **2003**, *53*, 27–62. [[CrossRef](#)]
55. Andersson, J.; Moller, C.; Johansson, L. Zircon geochronology of migmatite gneisses along the Mylonite Zone (S Sweden): A major Sveconorwegian terrane boundary in the Baltic Shield. *Precambrian Res.* **2002**, *114*, 121–147. [[CrossRef](#)]
56. Yu, S.Y.; Zhang, J.X.; Li, S.Z.; Sun, D.Y.; Li, Y.S.; Peng, Y.B. “Barrovian-type” metamorphism and in situ anatexis during continental collision: A case study from the South Altun Mountains, Western China. *Acta Pet. Sin.* **2016**, *32*, 3703–3714. (In Chinese)
57. Kemp, A.I.S.; Hawkesworth, C.J.; Collins, W.J.; Gray, C.M.; Blevin, P.L. Isotopic evidence for rapid continental growth in an extensional accretionary orogen: The Tasmanides, Eastern Australia. *Earth Planet. Sci. Lett.* **2009**, *284*, 455–466. [[CrossRef](#)]
58. Kemp, A.I.S.; Hawkesworth, C.J.; Paterson, B.A.; Kinny, P.D. Episodic growth of the Gondwana supercontinent from hafnium and oxygen isotopes in zircon. *Nature* **2006**, *439*, 580–583. [[CrossRef](#)] [[PubMed](#)]
59. Kemp, A.I.S.; Hickman, A.H.; Kirkland, C.L.; Vervoort, J.D. Hf isotopes in detrital and inherited zircons of the Pilbara Craton provide no evidence for Hadean continents. *Precambrian Res.* **2015**, *261*, 112–126. [[CrossRef](#)]
60. Lin, T.H.; Chung, S.L.; Chiu, H.Y.; Wu, F.Y.; Yeh, M.W.; Searle, M.P.; Iizuka, Y. Zircon U–Pb and Hf isotope constraints from the Ailao Shan–Red River shear zone on the tectonic and crustal evolution of southwestern China. *Chem. Geol.* **2012**, *291*, 23–37. [[CrossRef](#)]
61. Condie, K.C.; Beyer, E.; Belousova, E.; Griffin, W.L.; O'Reilly, S.Y. U–Pb isotopic ages and Hf isotopic composition of single zircons: The search for juvenile Precambrian continental crust. *Precambrian Res.* **2005**, *139*, 42–100. [[CrossRef](#)]
62. Jiang, N.; Guo, J.H.; Zhai, M.G.; Zhang, S.Q. ~2.7 Ga crust growth in the North China craton. *Precambrian Res.* **2010**, *179*, 37–49. [[CrossRef](#)]
63. Geng, Y.S.; Du, L.L.; Ren, L.D. Growth and reworking of the early Precambrian continental crust in the North China Craton: Constraints from zircon Hf isotopes. *Gondwana Res.* **2012**, *21*, 517–529. [[CrossRef](#)]
64. Vervoort, J.D.; Blichert-Toft, J. Evolution of the depleted mantle: Hf isotope evidence from juvenile rocks through time. *Geochim. Cosmochim. Acta* **1999**, *63*, 533–556. [[CrossRef](#)]
65. Blichert-Toft, J.; Albarède, F. The Lu–Hf isotope geochemistry of chondrites and the evolution of the mantle–crust system. *Earth Planet. Sci. Lett.* **1997**, *148*, 243–258. [[CrossRef](#)]
66. Tang, Z.L. *Metallogenic Systems and Metalotectonic Dynamics in the Southwest Margin (The Longshou Shan Mountains and the Qilianshan Mountains) of North China Palecontinent*; Geological Publishing House: Beijing, China, 2002. (In Chinese)
67. Li, B.; Jiang, S.Y.; Zhang, Q.; Zhao, H.X.; Zhao, K.D. Cretaceous crust–mantle interaction and tectonic evolution of Cathaysia Block in South China: Evidence from pulsed mafic rocks and related magmatism. *Tectonophysics* **2015**, *661*, 136–155. [[CrossRef](#)]
68. Hergt, J.M.; Peate, D.W.; Hawkesworth, C.J. The petrogenesis of Mesozoic Gondwana low-Ti flood basalts. *Earth Planet. Sci. Lett.* **1991**, *105*, 134–148. [[CrossRef](#)]
69. Meng, E.; Liu, F.L.; Liu, P.H.; Liu, C.H.; Yang, H.; Wang, F.; Shi, J.R.; Cai, J. Petrogenesis and tectonic significance of Paleoproterozoic meta-mafic rocks from central Liaodong Peninsula, northeast China: Evidence from zircon U–Pb dating and in situ Lu–Hf isotopes, and whole-rock geochemistry. *Precambrian Res.* **2014**, *247*, 92–109. [[CrossRef](#)]

70. Xiao, B.; Chen, H.Y.; Hollings, P.; Han, J.S.; Wang, Y.F.; Yang, J.T.; Cai, K.D. Magmatic evolution of the Tuwu-Yandong porphyry Cu belt, NW China: Constraints from geochronology, geochemistry and Sr-Nd-Hf isotopes. *Gondwana Res.* **2017**, *43*, 74–91. [[CrossRef](#)]
71. Ma, L.; Jiang, S.Y.; Hou, M.L.; Dai, B.Z.; Jiang, Y.H.; Yang, T.; Zhao, K.D.; Pu, W.; Zhu, Z.Y.; Xu, B. Geochemistry of Early Cretaceous calc-alkaline lamprophyres in the Jiaodong Peninsula: Implication for lithospheric evolution of the eastern North China Craton. *Gondwana Res.* **2014**, *25*, 859–872. [[CrossRef](#)]
72. Shu, S.Y.; Yang, X.Y.; Liu, L.; Lu, W.; Cao, J.Y.; Gao, E.G. Dual Geochemical Characteristics for the Basic Intrusions in the Yangtze Block, South China: New Evidence for the Breakup of Rodinia. *Minerals* **2018**, *8*, 228. [[CrossRef](#)]
73. Taylor, S.R.; McLennan, S.M.; Armstrong, R.L.; Tarney, J. The composition and evolution of the continental crust: Rare earth element evidence from sedimentary rocks. *Philos. Trans. R. Soc. Lond.* **1981**, *301*, 381–399. [[CrossRef](#)]
74. Chi, Q.H.; Yan, M.C. *Handbook of Elemental Abundance for Applied Geochemistry*; Geological Publishing House: Beijing, China, 2007. (In Chinese)
75. Wang, K.X.; Sun, T.; Chen, P.R.; Ling, H.F.; Xiang, T.F. The geochronological and geochemical constraints on the petrogenesis of the Early Mesozoic A-type granite and diabase in northwestern Fujian province. *Lithos* **2013**, *179*, 364–381. [[CrossRef](#)]
76. Cao, J.; Ye, H.S.; Chen, X.D.; He, W.; Wang, P. Geochemistry, zircon U–Pb age, and Lu–Hf isotope of the granite porphyry in Leimengou Mo deposit in the east Qinling Molybdenum ore belt, China. *Minerals* **2018**, *8*, 293. [[CrossRef](#)]
77. Watson, E.B.; Harrison, T.M. Zircon saturation revisited: Temperature and composition effects in a variety of crustal magma types. *Earth Planet. Sci. Lett.* **1983**, *64*, 295–304. [[CrossRef](#)]
78. Skjerlie, K.P.; Johnston, A.D. Vapor-absent melting at 10 kbar of a biotite-and amphibole-bearing tonalitic gneiss: Implications for the generation of A-type granites. *Geology* **1992**, *20*, 263–266. [[CrossRef](#)]
79. Douce, A.E.P. Generation of metaluminous A-type granites by low-pressure melting of calc-alkaline granitoids. *Geology* **1997**, *25*, 743–746. [[CrossRef](#)]
80. Wolf, M.B.; London, D. Apatite dissolution into peraluminous haplogranitic melts: An experimental study of solubilities and mechanisms. *Geochim. Cosmochim. Acta* **1994**, *58*, 4127–4145. [[CrossRef](#)]
81. Whalen, J.B.; Currie, K.L.; Chappell, B.W. A-type granites: Geochemical characteristics, discrimination and petrogenesis. *Contrib. Miner. Pet.* **1987**, *95*, 407–419. [[CrossRef](#)]
82. Eby, G.N. The A-type granitoids: A review of their occurrence and chemical characteristics and speculations on their petrogenesis. *Lithos* **1990**, *26*, 115–134. [[CrossRef](#)]
83. Yang, L.Z.; Wu, X.B.; Cao, J.Y.; Hu, B.; Zhang, X.W.; Gong, Y.S.; Liu, W.D. Geochronology, Petrology, and Genesis of Two Granitic Plutons of the Xianghualing Ore Field in South Hunan Province: Constraints from Zircon U–Pb Dating, Geochemistry, and Lu–Hf Isotopic Compositions. *Minerals* **2018**, *8*, 213. [[CrossRef](#)]
84. Eby, G.N. Chemical subdivision of the A-type granitoids: Petrogenetic and tectonic implications. *Geology* **1992**, *20*, 641–644. [[CrossRef](#)]
85. Wu, F.Y.; Sun, D.Y.; Li, H.M.; Jahn, B.M.; Wilde, S. A-type granites in northeastern China: Age and geochemical constraints on their petrogenesis. *Chem. Geol.* **2002**, *187*, 143–173. [[CrossRef](#)]
86. Du, L.L.; Yang, C.H.; Wang, W.; Ren, L.D.; Wan, Y.S.; Wu, J.S.; Zhao, L.; Song, H.X.; Geng, Y.S.; Hou, K.J. Paleoproterozoic rifting of the North China Craton: Geochemical and zircon Hf isotopic evidence from the 2137 Ma Huangjinshan A-type granite porphyry in the Wutai area. *J. Asian Earth Sci.* **2013**, *72*, 190–202. [[CrossRef](#)]
87. Clemens, J.D.; Holloway, J.R.; White, A.J.R. Origin of an A-type granite: Experimental constraints. *Am. Miner.* **1986**, *71*, 317–324.
88. King, P.L.; Chappell, B.W.; Allen, C.M.; White, A.J.R. Are A-type granites the high-temperature felsic granites? Evidence from fractionated granites of the Wangrah Suite. *Aust. J. Earth Sci.* **2001**, *48*, 501–514. [[CrossRef](#)]
89. Zheng, Y.F.; Wu, Y.B.; Zhao, Z.F.; Zhang, S.; Xu, P.; Wu, F. Metamorphic effect on zircon Lu–Hf and U–Pb isotope systems in ultrahigh-pressure eclogite-facies metagranite and metabasite. *Earth Planet. Sci. Lett.* **2005**, *240*, 378–400. [[CrossRef](#)]
90. Wu, F.Y.; Liu, X.C.; Ji, W.Q.; Wang, J.M.; Yang, L. Highly fractionated granites: Recognition and research. *Sci. China Earth Sci.* **2017**, *7*, 1–19. [[CrossRef](#)]

91. Chen, G.N.; Grapes, R. *Granite Genesis: In Situ Melting and Crusta Evolution*; Springer: Dordrecht, The Netherlands, 2007.
92. Zhai, M.G.; Peng, P. Paleoproterozoic events in the North China craton. *Acta Pet. Sin.* **2007**, *23*, 2665–2682. (In Chinese)
93. Zhai, M.G. Cratonization and the Ancient North China Continent: A summary and review. *Sci. China Earth Sci.* **2011**, *54*, 1110–1120. [[CrossRef](#)]
94. Liu, Y. Characteristics and Their Geological Significance of Paleoproterozoic Granite in Jinchuan, Gansu Province. Master's Thesis, China University of Geosciences, Beijing, China, 2008. (In Chinese)
95. Wang, Q. Study on Metamorphism of Longshoushan Baijiazuzi Group. Master's Thesis, Chang'an University, Xi'an, China, 2014. (In Chinese)
96. Loiselle, M.C.; Wones, D.R. Characteristics and origin of anorogenic granites. *Geol. Soci. Am. Abstr. Programs* **1979**, *11*, 468.
97. Whalen, J.B.; Jenner, G.A.; Longstaffe, F.J.; Robert, F.; Gariépy, C. Geochemical and isotopic (O, Nd, Pb and Sr) constraints on A-type granite petrogenesis based on the Topsails igneous suite, Newfoundland Appalachians. *J. Pet.* **1996**, *37*, 1463–1489. [[CrossRef](#)]
98. Pearce, J.A.; Norry, M.J. Petrogenetic implications of Ti, Zr, Y, and Nb variations in volcanic rocks. *Contrib. Miner. Pet.* **1979**, *69*, 33–47. [[CrossRef](#)]
99. Sun, S.Q.; Zhang, C.; Zhao, S. Identification of the tectonic settings for continental intraplate by trace elements. *Geotecton. Metallog.* **2007**, *31*, 104–109.
100. Condie, K.C. Geochemical changes in basalts and andesites across the Archean-Proterozoic boundary: Identification and significance. *Lithos* **1989**, *23*, 1–18. [[CrossRef](#)]
101. Shervais, J.W. Ti-V plots and the petrogenesis of modern and ophiolitic lavas. *Earth Planet. Sci. Lett.* **1982**, *59*, 101–118. [[CrossRef](#)]
102. Wu, Y.B.; Zheng, Y.F.; Zhang, S.B.; Zhao, Z.F.; Wu, F.Y.; Liu, X.M. Zircon U–Pb ages and Hf isotope compositions of migmatite from the North Dabie terrane in China: Constraints on partial melting. *J. Metamorph. Geol.* **2007**, *25*, 991–1009. [[CrossRef](#)]
103. Villaseca, C.; Romera, C.M.; Barbero, L. Melts and residua geochemistry in a low-to-mid crustal section (Central Spain). *Phys. Chem. Earth Part A Solid Earth Geodesy* **2001**, *26*, 273–280. [[CrossRef](#)]
104. Liu, F.L.; Robinson, P.T.; Gerdes, A.; Xue, H.M.; Liu, P.H.; Liou, J.G. Zircon U–Pb ages, REE concentrations and Hf isotope compositions of granitic leucosome and pegmatite from the north Sulu UHP terrane in China: Constraints on the timing and nature of partial melting. *Lithos* **2010**, *117*, 247–268. [[CrossRef](#)]
105. Liu, F.L.; Robinson, P.T.; Liu, P.H. Multiple partial melting events in the Sulu UHP terrane: Zircon U–Pb dating of granitic leucosomes within amphibolite and gneiss. *J. Metamorph. Geol.* **2012**, *30*, 887–906. [[CrossRef](#)]
106. Aikman, A.B.; Harrison, T.M.; Lin, D. Evidence for Early (>44 Ma) Himalayan Crustal Thickening, Tethyan Himalaya, southeastern Tibet. *Earth Planet. Sci. Lett.* **2008**, *274*, 14–23. [[CrossRef](#)]
107. Zeng, L.S.; Gao, L.E.; Xie, K.J.; Liu, Z.J. Mid-Eocene high Sr/Y granites in the Northern Himalayan Gneiss Domes: Melting thickened lower continental crust. *Earth Planet. Sci. Lett.* **2011**, *303*, 251–266. [[CrossRef](#)]
108. Rubatto, D.; Chakraborty, S.; Dasgupta, S. Timescales of crustal melting in the Higher Himalayan Crystallines (Sikkim, Eastern Himalaya) inferred from trace element-constrained monazite and zircon chronology. *Contrib. Miner. Pet.* **2013**, *165*, 349–372. [[CrossRef](#)]
109. Hou, G.T.; Santosh, M.; Qian, X.L.; Lister, G.S.; Li, J.H. Configuration of the Late Paleoproterozoic supercontinent Columbia: Insights from radiating mafic dyke swarms. *Gondwana Res.* **2008**, *14*, 395–409. [[CrossRef](#)]
110. Condie, K.C.; Aster, R.C. Episodic zircon age spectra of orogenic granitoids: The supercontinent connection and continental growth. *Precambrian Res.* **2010**, *180*, 227–236. [[CrossRef](#)]
111. Zhao, G.C.; Cawood, P.A. Precambrian geology of China. *Precambrian Res.* **2012**, *222*, 13–54. [[CrossRef](#)]
112. Guo, J.H.; Zhai, M.G.; Xu, R.H. Timing of the granulite facies metamorphism in the Sanggan area, North China craton: Zircon U–Pb geochronology. *Sci. China* **2001**, *44*, 1010–1018. [[CrossRef](#)]
113. Geng, Y.S.; Zhou, X.W.; Wang, X.S.; Ren, L.D. Late-Paleoproterozoic granite events and their geological significance in Helanshan area, Inner Mongolia: Evidence from geochronology. *Acta Pet. Sin.* **2009**, *25*, 1830–1842. (In Chinese)

114. Wan, Y.S.; Xu, Z.Y.; Dong, C.Y.; Nutman, A.; Ma, M.Z.; Xie, H.Q.; Liu, S.J.; Liu, D.Y.; Wang, H.C.; Cu, H. Episodic Paleoproterozoic (~2.45, ~1.95 and ~1.85 Ga) mafic magmatism and associated high temperature metamorphism in the Daqingshan area, North China Craton: SHRIMP zircon U–Pb dating and whole-rock geochemistry. *Precambrian Res.* **2013**, *224*, 71–93. [[CrossRef](#)]
115. Dan, W.; Li, X.H.; Wang, Q.; Wang, X.C.; Liu, Y.; Wyman, D.A. Paleoproterozoic S-type granites in the Helanshan Complex, Khondalite Belt, North China Craton: Implications for rapid sediment recycling during slab break-off. *Precambrian Res.* **2014**, *254*, 59–72. [[CrossRef](#)]
116. Guo, J.H.; O'Brien, P.J.; Zhai, M. High-pressure granulites in the Sanggan area, North China craton: Metamorphic evolution, P–T paths and geotectonic significance. *J. Metamorph. Geol.* **2002**, *20*, 741–756.
117. Peng, P.; Zhai, M.G.; Zhang, H.F.; Guo, J.H. Geochronological constraints on the Paleoproterozoic evolution of the North China Craton: SHRIMP zircon ages of different types of mafic dikes. *Int. Geol. Rev.* **2005**, *47*, 492–508. [[CrossRef](#)]
118. Dong, C.Y.; Wan, Y.S.; Xu, Z.Y.; Liu, D.Y.; Yang, Z.S.; Ma, M.Z.; Xie, H.Q. SHRIMP zircon U–Pb dating of late Paleoproterozoic kandalites in the Daqing Mountains area on the North China Craton. *Sci. China Earth Sci.* **2013**, *56*, 115–125. [[CrossRef](#)]
119. Yin, C.Q.; Zhao, G.C.; Guo, J.H.; Sun, M.; Xia, X.P.; Zhou, X.W.; Liu, C.H. U–Pb and Hf isotopic study of zircons of the Helanshan Complex: Constrains on the evolution of the Khondalite Belt in the Western Block of the North China Craton. *Lithos* **2011**, *122*, 25–38. [[CrossRef](#)]
120. Yin, C.Q.; Zhao, G.C.; Sun, M.; Xia, X.P.; Wei, C.J.; Zhou, X.W.; Leung, W.H. LA-ICP-MS U–Pb zircon ages of the Qianlishan Complex: Constrains on the evolution of the Khondalite Belt in the Western Block of the North China Craton. *Precambrian Res.* **2009**, *174*, 78–94. [[CrossRef](#)]
121. Jian, P.; Kröner, A.; Windley, B.F.; Zhang, Q.; Zhang, W.; Zhang, L.Q. Episodic mantle melting-crustal reworking in the late Neoproterozoic of the northwestern North China Craton: Zircon ages of magmatic and metamorphic rocks from the Yinshan Block. *Precambrian Res.* **2012**, *222–223*, 230–254. [[CrossRef](#)]
122. Jian, P.; Zhang, Q.; Liu, D.Y.; Jin, W.J.; Jia, X.Q.; Qian, Q. SHRIMP dating and geological significance of Late Achaean high-Mg diorite (sanukite) and hornblende-granite at Guyang of Inner Mongolia. *Acta Pet. Sin.* **2005**, *21*, 151–157. (In Chinese)
123. Dong, X.J.; Xu, Z.Y.; Liu, Z.H.; Sha, Q. Zircon U–Pb geochronology of Archean high-grade metamorphic rocks from Xi Ulanbulang area, central Inner Mongolia. *Sci. China Earth Sci.* **2012**, *55*, 204–212. [[CrossRef](#)]
124. Ma, X.D.; Guo, J.H.; Liu, F.; Qian, Q.; Fan, H.R. Zircon U–Pb ages, trace elements and Nd–Hf isotopic geochemistry of Guyang sanukitoids and related rocks: Implications for the Archean crustal evolution of the Yinshan Block, North China Craton. *Precambrian Res.* **2013**, *230*, 61–78. [[CrossRef](#)]



© 2018 by the authors. Licensee MDPI, Basel, Switzerland. This article is an open access article distributed under the terms and conditions of the Creative Commons Attribution (CC BY) license (<http://creativecommons.org/licenses/by/4.0/>).